# Holocene Paleoseismology of the Steamboat Mountain Site: Evidence for Full-Length Rupture of the Teton Fault, Wyoming

Christopher B. DuRoss\*1, Mark S. Zellman2, Glenn D. Thackray3, Richard W. Briggs1, Ryan D. Gold1, and Shannon A. Mahan<sup>4</sup>

### ABSTRACT -

The 72-km-long Teton fault in northwestern Wyoming is an ideal candidate for reconstructing the lateral extent of surface-rupturing earthquakes and testing models of normal-fault segmentation. To explore the history of earthquakes on the northern Teton fault, we handexcavated two trenches at the Steamboat Mountain site, where the east-dipping Teton fault has vertically displaced west-sloping alluvial-fan surfaces. The trenches exposed glaciofluvial, alluvial-fan, and scarp-derived colluvial sediments and stratigraphic and structural evidence of two surface-rupturing earthquakes (SM1 and SM2). A Bayesian geochronologic model for the site includes three optically stimulated luminescence ages (~12-17 ka) for the glaciofluvial units and 16 radiocarbon ages (~1.2-8.6 ka) for the alluvial-fan and colluvial units and constrains SM1 and SM2 to  $5.5 \pm 0.2$  ka,  $1\sigma$  (5.2–5.9 ka, 95%) and  $9.7 \pm 0.9$  ka,  $1\sigma$  (8.5–11.5 ka, 95%), respectively. Structural, stratigraphic, and geomorphic relations yield vertical displacements for SM1  $(2.0 \pm 0.6 \text{ m}, 1\sigma)$  and SM2  $(2.0 \pm 1.0 \text{ m}, 1\sigma)$ . The Steamboat Mountain paleoseismic chronology overlaps temporally with earthquakes interpreted from previous terrestrial and lacustrine paleoseismic data along the fault. Integrating these data, we infer that the youngest Teton fault rupture occurred at ~5.3 ka, generated 1.7  $\pm$  1.0 m, 1 $\sigma$  of vertical displacement along 51–70 km of the fault, and had a moment magnitude ( $M_{\rm w}$ ) of ~7.0–7.2. This rupture was apparently unimpeded by structural complexities along the Teton fault. The integrated chronology permits a previous full-length rupture at ~10 ka and possible partial ruptures of the fault at ~8-9 ka. To reconcile conflicting terrestrial and lacustrine paleoseismic data, we propose a hypothesis of alternating full- and partial-length ruptures of the Teton fault, including  $M_{\rm w}$  ~6.5–7.2 earthquakes every ~1.2 ky. Additional paleoseismic data for the northern and central sections of the fault would serve to test this bimodal rupture hypothesis.

### **KEY POINTS**

- Trenches across the northern Teton fault at Steamboat Mountain yield evidence of two postglacial earthquakes.
- Paleoseismic data indicate a full-length (51–70-km-long),  $M_{\rm w}$  7.0–7.2 rupture of the Teton fault at ~5.3 ka.
- We reconcile terrestrial and lacustrine data and propose a model of bimodal (full and partial) fault rupture.

**Supplemental Material** 

### **INTRODUCTION**

Paleoseismic rupture histories derived from point observations of earthquake timing and displacement (Biasi and Weldon, 2009; Scharer et al., 2014; DuRoss et al., 2016; Scharer and Yule, 2020) are well suited to address open questions regarding whether complex along-strike fault geometries and structures

act as barriers to rupture (Schwartz and Coppersmith, 1984) and provide critical inputs to probabilistic seismic hazard assessment (e.g., Field et al., 2014; Petersen et al., 2019). Potential barriers to rupture likely fall on a spectrum from persistent or frequent (strong structural control on rupture) to ephemeral (weak or inconsistent control on rupture) (Philibosian and Meltzner, 2020). Similarly, fault segmentation constraints in earthquake hazard models range from fully segmented, where

Cite this article as DuRoss, C. B., M. S. Zellman, G. D. Thackray, R. W. Briggs, R. D. Gold, and S. A. Mahan (2020). Holocene Paleoseismology of the Steamboat Mountain Site: Evidence for Full-Length Rupture of the Teton Fault, Wyoming, Bull. Seismol. Soc. Am. XX, 1-27, doi: 10.1785/0120200212

© Seismological Society of America

<sup>1.</sup> U.S. Geological Survey, Golden, Colorado, U.S.A.; 2. BGC Engineering, Inc., Golden, Colorado, U.S.A.; 3. Department of Geosciences, Idaho State University, Pocatello, Idaho, U.S.A.; 4. U.S. Geological Survey, Denver Federal Center, Denver, Colorado, U.S.A.

<sup>\*</sup>Corresponding author: cduross@usgs.gov

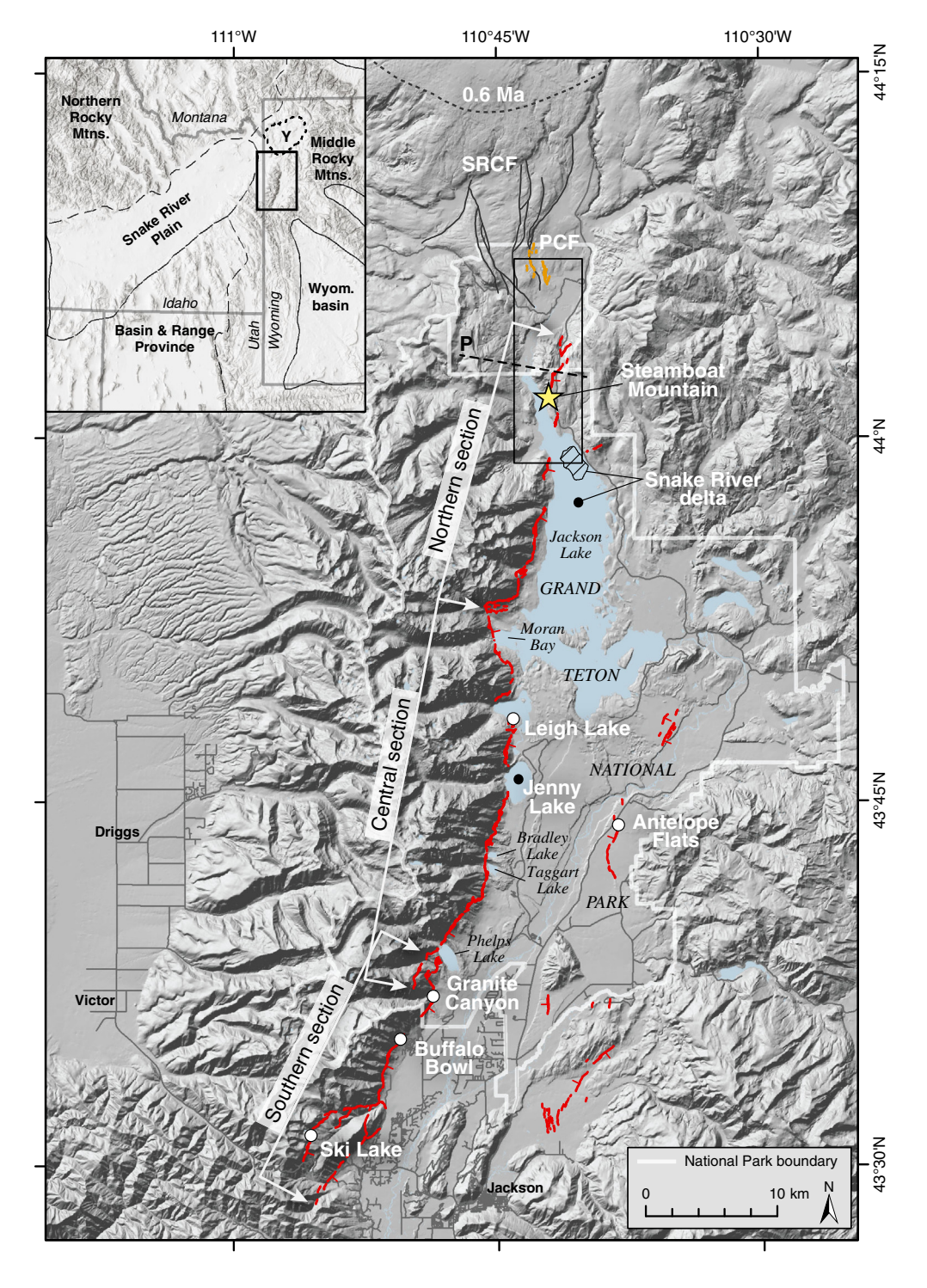


**Figure 1.** The Teton fault, showing the Steamboat Mountain paleoseismic site (star) and previous paleoseismic trenching studies (white circles) at the Granite Canyon (Byrd, 1995), Leigh Lake (Zellman, DuRoss, Thackray, et al., 2019), and Buffalo Bowl (DuRoss et al., 2019) sites. Additional data include lacustrine disturbance horizons (turbidites) from Jenny Lake (Larsen et al., 2019) and geomorphic evidence of earthquakes along the Snake River delta (Pierce et al., 1998). Paleoseismic data for the Antelope Flats and Ski Lake sites were not available at the time of this study. Surface traces of the Teton fault and Polecat Creek faults (PCF), which form the southern part of the Snake River caldera faults (SRCF; Machette et al., 2001), are from Zellman, DuRoss, and Thackray (2019). Dashed line shows topographic profile (P) across the northern Teton fault (Fig. 2). Dotted line shows faults along the Lava Creek caldera (Machette et al., 2001), which define the 0.6 Ma Yellowstone caldera boundary (Christiansen, 1984, 2001; Machette et al., 2001). Rectangle shows extent of Figure 2a. Inset map shows physiographic provinces and the Yellowstone caldera (Y); rectangle shows area of this figure. The color version of this figure is available only in the electronic edition.

hard rupture boundaries yield spatially similar rupture parameters (Working Group on Utah Earthquake Probabilities, 2016; Petersen et al., 2019) to penalized, where less persistent rupture boundaries add variability in rupture length and magnitude (e.g., Valentini et al., 2019), and to unsegmented, where ruptures unconstrained by geometric complexities yield the largest suite of possible ruptures (e.g., Field et al., 2014). Notably, differences in hazard across these models can surpass other sources of uncertainty, such as deformation (e.g., slip rate) models and choice of magnitude-length scaling relations (Valentini et al., 2019). As a result, defining the spatial limits and associated uncertainties of prehistoric ruptures in concert with the assessment of fault-slip rate and earthquake recurrence is essential to improve the accuracy of regional seismic hazard analyses.

The Teton fault in northwest Wyoming (Fig. 1) represents an ideal candidate for testing models of fault segmentation and using paleoseismic data to evaluate along-strike rupture extent. The 72 km long fault (Zellman, DuRoss, Thackray, 2019) has geologic and geomorphic evidence of postglacial (Licciardi and Pierce, 2018; Pierce et al., 2018) surface-faulting earthquakes (Gilbert et al., 1983; Smith et al., 1993; Byrd et al., 1994; Byrd, 1995; O'Connell et al., 2003; Thackray and Staley, 2017; DuRoss et al., 2019; Zellman, DuRoss, Thackray, et al., 2019) and is composed of at least three geometric sections that are  $\sim$ 20–30 km in length (Smith et al., 1993; O'Connell et al., 2003; DuRoss et al., 2019).

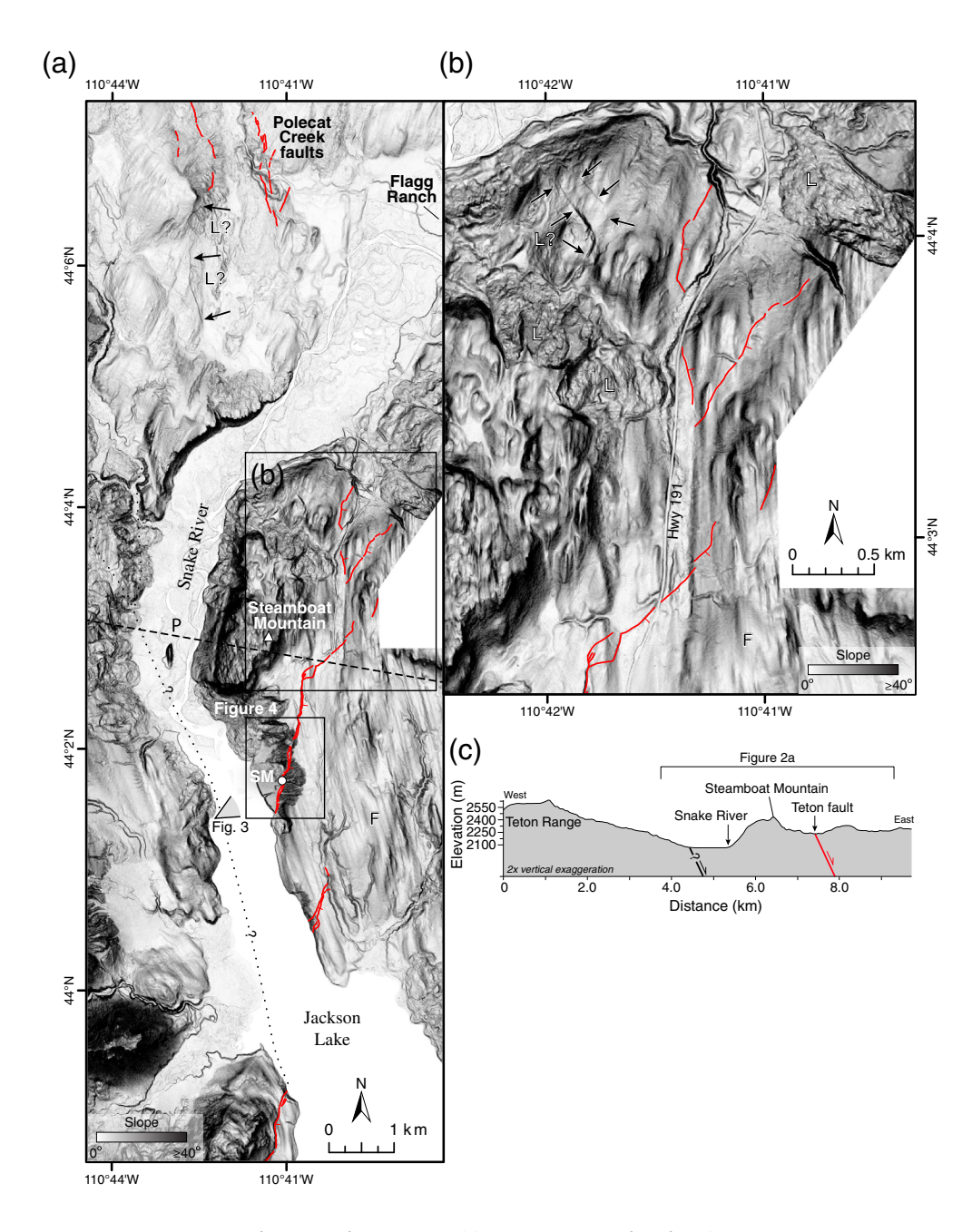


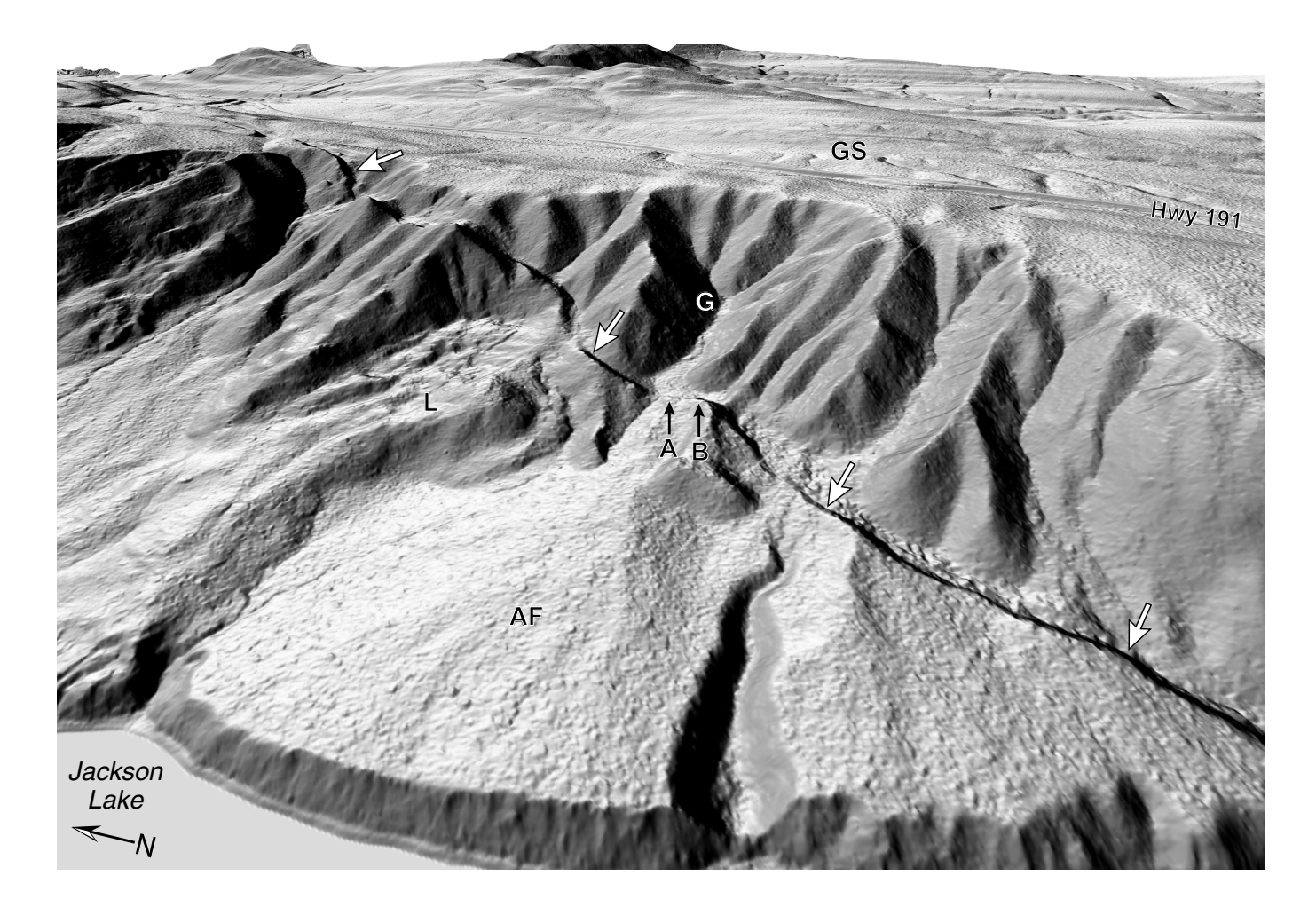
**Figure 2.** Northern extent of the Teton fault, showing (a) northern ~5 km of the fault (solid lines—Zellman, DuRoss, and Thackray, 2019; dotted lines show inferred trace from Love *et al.*, 1992) from Jackson Lake to (b) the northern terminus of the fault with glacial morphology, such as fluting (F) crosscut by Teton fault scarps. Arrows in (a) denote scarps associated with either landslides or the southern terminus of the Polecat Creek faults. Scarps marked by arrows in (b) are likely related to landsliding or could be the evidence of distributed and disconnected surface faulting along the northernmost Teton fault. No scarps are present along the Snake River floodplain or its margins. L, landslide deposits; SM, Steamboat Mountain trench site. Fault mapping from Zellman, DuRoss, and Thackray (2019). (c) Topographic profile (P) across the Teton fault, showing possible subsurface geometry and queried ancestral Teton fault west of Steamboat Mountain (after Love *et al.*, 1992). Profile location shown in Figure 1. Basemap is 1 m light detection and ranging (lidar) slopeshade. The color version of this figure is available only in the electronic edition.

The degree to which ruptures along the fault are influenced by along-strike geometric complexities remains an open question. Similar earthquake-timing results for the southern and central

sections of the fault suggest that ruptures could equal or exceed ~46 km in length (DuRoss et al., 2019; Zellman, DuRoss, Thackray, et al., 2019), consistent with full-length ruptures of the fault (55-62 km; moment magnitude  $[M_w] \sim 7.2$ ) included in the hazard models of White et al. (2009) and Petersen et al. (2014, 2019). However, these data, as well as lacustrine paleoseismic data (Larsen et al., 2019), also allow for shorter, partial ruptures of the fault possibly restricted laterally by the fault section boundaries (DuRoss et al., 2019).

In this article, we present new paleoseismic data for the Steamboat Mountain site on the northern section of the Teton fault (Fig. 2). No trenches have previously been excavated across the 20 km long northern section; thus, our goal is to explore the timing and spatial extent of the youngest surfacefaulting earthquakes along this part of the fault. We excavated two trenches across an uphillfacing fault scarp that traps alluvial-fan sediments on the hanging wall of the fault at the mouth of a west-sloping drainage (Fig. 2). Herein, we (1) present stratigraphic and geochronologic data from two trenches across the northern Teton fault, (2) discuss evidence in support of two Holocene surface-faulting ruptures, (3) use Bayesian modeling to constrain the timing of these earthquakes, and (4) synthesize paleoseismic data along the length of the Teton fault to resolve the timdisplacement, rupture ing, length, and magnitude of the youngest Teton fault rupture.

Our results suggest that at least two ruptures of the northernmost Teton fault have occurred since  $\sim$ 12 ka, including a full-length rupture of the fault at  $\sim$ 5.3 ka in an  $M_{\rm w} \sim$ 7.0–7.2 earthquake.



### **TECTONIC SETTING**

The Teton fault accommodates southwest–northeast extension across the northern portion of the Basin and Range Province (Smith *et al.*, 1993; Fig. 1) and is one of the fastest-slipping and most hazardous normal faults in the Intermountain West (White *et al.*, 2009). The fault dips ~45°–75° east beneath Jackson Hole (Lageson, 1992; Byrd *et al.*, 1994; DuRoss *et al.*, 2019) and has resulted in 6–9 km of throw since ~5–13 Ma (Smith *et al.*, 1993; Brown *et al.*, 2017), contributing to the prominent (~2.2-km-high) vertical relief of the Teton Range. Recent fault movement is demonstrated by the vertical displacement of geomorphic surfaces associated with Pinedale glaciation (~13–16 ka; Licciardi and Pierce, 2018; Pierce *et al.*, 2018). These surfaces are displaced as much as 10–14 m and yield postglacial vertical slip rates of ~1 mm/yr (Thackray and Staley, 2017; DuRoss *et al.*, 2019).

The 72 km long Teton fault (Zellman, DuRoss, and Thackray, 2019) extends from the Yellowstone caldera to the north to thrust faults of the Laramide orogeny to the south (Smith *et al.*, 1990, 1993; Lageson, 1992; Fig 1). At its south end, the Teton fault likely terminates at a 90° intersection with the northwest-striking and northeast-dipping Cache Creek thrust (Lageson, 1992; Smith *et al.*, 1993). This southern termination corresponds with the southern extent of mapped fault scarps

**Figure 3.** Oblique east-northeast view of the Steamboat Mountain site, showing the approximate location of trenches A and B. Large arrows indicate prominent east-facing fault scarps. Geomorphic features near the site include an alluvial-fan (AF) surface on the fault hanging wall, an erosional gully (G) in the footwall, a glaciated surface (GS) with Jackson Lake lobe moraine deposits above the site, and a landslide (L) to the north. Basemap is 1 m lidar data, with a 315° sun-illumination angle. Scale varies across the image; however, the total fault length between white arrows is  $\sim$ 1 km.

(Smith *et al.*, 1990, 1993; Zellman, DuRoss, and Thackray, 2019) and an abrupt decrease in the height of the Teton Range (Lageson, 1992). At the north end, the northernmost scarps associated with the Teton fault are north of Jackson Lake and east of the Snake River (Smith *et al.*, 1993; Machette *et al.*, 2001; Zellman, DuRoss, and Thackray, 2019), 20–25 km south of the ~0.6 Ma Yellowstone caldera boundary (Fig. 1), and approximately coincident with the southern margin of the 2.1 Ma Yellowstone caldera boundary (Christiansen, 1984, 2001; Smith and Braile, 1994; Smith *et al.*, 2009).

### **Northern Teton fault**

The northern section of the Teton fault extends for 20 km from a prominent along-strike bend near Moran Bay in Jackson Lake

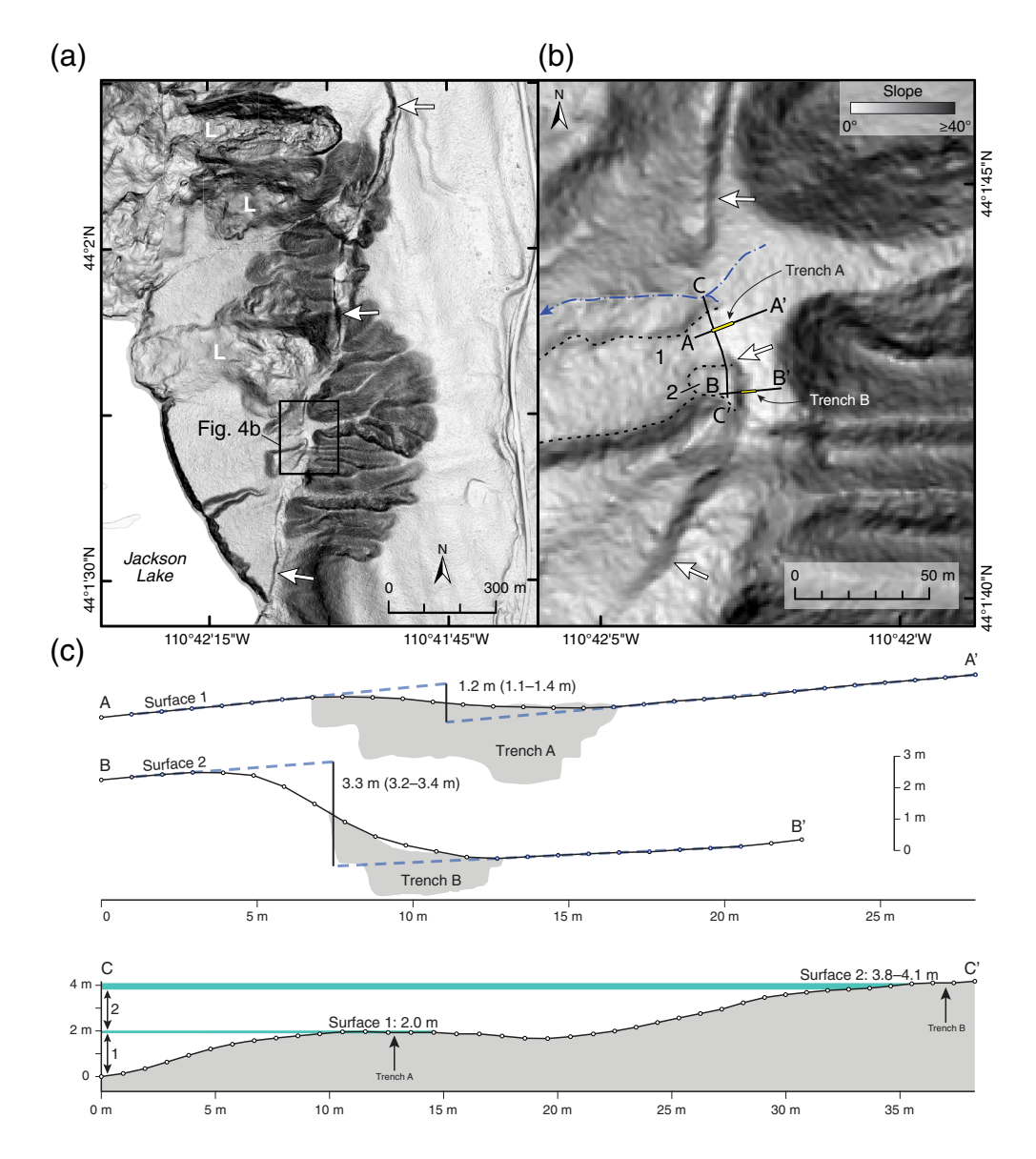


Figure 4. (a) The expression of the Teton fault northeast of Jackson lake; arrows indicate prominent east-facing fault scarps. L, landslide deposits. (b) The Steamboat Mountain site, showing modern stream channel (dashed-dotted line), uplifted alluvial-fan surfaces 1 and 2 outlined by dotted lines, and trenches A and B. Arrows show east-facing fault scarps. Basemaps depict slope for 1 m lidar data acquired by Grand Teton National Park in 2014. (c) Topographic profiles across to the Teton fault scarp, showing the extent of trenches A and B. Dashed lines show vertical separation across the Teton fault scarp. In fault-parallel profile C-C', horizontal lines show height of fluvial surfaces 1 and 2 above the modern stream channel and indicate progressive offset (footwall uplift) across the fault. No vertical exaggeration. The color version of this figure is available only in the electronic edition.

to the northern terminus of the fault near Steamboat Mountain (Smith et al., 1993; O'Connell et al., 2003; Zellman, DuRoss, and Thackray, 2019; Fig. 1). The fault bend consists of a 2.5-km-wide underlapping step in the fault trace, which is linked by a zone of east-west-striking cross faults (Zellman, DuRoss, and Thackray, 2019). From this bend north to the point at which it continues beneath Jackson Lake, the Teton fault is expressed by a northnortheast-trending alignment of fault scarps that vertically displace late-Pleistocene glacial deposits and landforms. The fault

intersects the western margin of Jackson Lake (Fig. 1) as a single strand, with ~6 m of vertical separation in undated Pleistocene glacial deposits. This contrasts with ~10-14 m vertical separation Holocene and older deposits on the southern and central sections of the fault (Thackray and Staley, 2017). The Teton fault continues north-northeast of Jackson Lake for ∼5 km (Fig 2a). The northern terminus of the fault is near Steamboat Mountain, where scarps bend to the northeast and horsetail into at least three strands, before becoming indistinguishable (Fig 2b).

Immediately northeast of Jackson Lake, the east-dipping Teton fault trends across a steep west-facing slope onto a glaciated surface ~150 m above the lake level (Figs. 3 and 4). The steep slope is scalloped by landslides, and west-sloping channels have incised into the Cretaceous sedimentary bedrock and overlying Tertiary rhyolite volcanic bedrock of Yellowstone volcanic sequence (Love et al., 1992; Fig. 3). This area is within the main inferred path of the Snake River lobe of Yellowstone plateau ice cap (Pierce et al., 2018), which scoured a deep glacial trough north of Jackson Lake in late Pinedale time  $(\sim 13-16 \text{ ka};$ Licciardi and Pierce, 2018) and deposited coarse glacial

sediments along its margins (Love et al., 1992; Pierce et al., 2018). In the study area, Pinedale glaciation is expressed in south- to south-southeast-trending drumlins. Between Jackson Lake and the glaciated surface, the Teton fault is expressed as uphill- (east-) facing fault scarps and a narrow (<50-m-wide), northeast-trending graben that has been locally scoured by axial streamflow (Fig. 4a). Landslides involving both volcanic bedrock and unconsolidated (including glacial) sediments are present near but mostly west of the Teton fault (Fig. 2). The northern ~5 km of the active Teton fault (north of Jackson Lake; solid lines, Fig. 2a) is unique as it deviates east from the base of the Teton Range (Fig. 2c). This geometry has resulted in clear evidence of faulting in Quaternary sediments, glacially scoured bedrock, and postglacial fan and hillslope landforms, including locally uphill-facing scarps northeast of Jackson Lake (Love et al., 1992; Smith et al., 1993; Zellman, DuRoss, and Thackray, 2019; Fig. 2a). Eastward migration of the Teton fault helps explain the lack of accumulated throw in the footwall of the Teton fault trace. The base of the Teton Range is ~2–3 km west of the Teton fault trace and could mark an abandoned ancestral trace (dotted lines, Fig. 2a) that is largely responsible for Teton Range uplift but is now buried beneath the Snake River floodplain (e.g., Love et al., 1992; Ostenaa et al., 1993; Fig. 2c).

### Previous paleoseismic data

Previous paleoseismic investigations of the Teton fault are concentrated on the southern and central sections (Fig. 1). These include the Buffalo Bowl (DuRoss et al., 2019), Granite Canyon (Byrd, 1995), and Leigh Lake (Zellman, DuRoss, Thackray, et al., 2019) sites, 25-50 km to the south of Steamboat Mountain. At the Buffalo Bowl site, three surface ruptures are constrained to ~9.9 ka (BB3; 9.4-10.4 at 95% confidence), ~7.1 ka (BB2; 5.5-8.8 ka; 95%), and ~4.6 ka (BB1; 3.9-5.7 ka; 95%). The Granite Canyon site exposed evidence of ruptures at ~8.1 ka (GC2; 7.9-8.4 ka; 95%) and ~6.3 ka (GC1; 4.8-7.8 ka; 95%) (GC1 and GC2 timing data are derived from a Bayesian model of the site included in DuRoss et al., 2019). At the Leigh Lake site, surface ruptures occurred at ~10.0 ka (LL2; 9.8-10.5 ka; 95%) and ~5.9 ka (LL1; 4.8-7.1; 95%). These earthquake histories suggest that at least three Holocene surface-faulting earthquakes at ~10, ~8, and ~5 ka have ruptured the fault; however, rupture lengths remain broadly constrained (DuRoss et al., 2019; Zellman, DuRoss, Thackray, et al., 2019). Additional paleoseismic data from trenches excavated at Ski Lake and Antelope Flats (Fig. 1) were not available at the time of this study.

Lacustrine paleoseismic data from Jenny Lake (Fig. 1) also provide evidence of large earthquakes. Larsen *et al.* (2016, 2019) used multibeam bathymetry, high-resolution seismic imaging, and coring to interpret basinwide disturbance horizons (turbidites) and landslides likely triggered by Teton fault ruptures. Jenny Lake sediment chronologies are constrained by radiocarbon dating, varve counting, and identification of rhyolitic tephra layers (i.e., ~13.6 ka Glacier Peak and ~7.6 ka Mazama tephra beds) and are interpreted to record seven earthquakes between ~14 and 8 ka (Larsen *et al.*, 2019). The youngest turbidite at ~5.3 ka is only weakly expressed in the Jenny Lake sediment. Seven <sup>10</sup>Be exposure ages from bedrock exposed in the landslide headscarp and boulders from landslide deposits adjacent to Jenny Lake corroborate the ~14 and ~8 ka lacustrine disturbance horizons.

Along the northern Teton fault, the geomorphology of the Snake River floodplain and delta surface (Fig. 1) provides indirect evidence of strong ground shaking, possibly as a result of large earthquakes on the Teton fault. Pierce et al. (1998) used kilometer-scale liquefaction features and geomorphic relations consistent with hanging-wall subsidence, as well as radiocarbon and archeological age constraints to interpret two late Holocene Teton fault earthquakes. These features are now submerged by Jackson Lake, but they were subaerially exposed prior construction of the Jackson Lake dam in 1916 and briefly re-exposed during repair work on the Jackson Lake dam (Pierce et al., 1998). DuRoss et al. (2019) used the age constraints in a Bayesian model, which yields possible earthquakes at ~4.5 ka (SRD2; 3.7-5.5 ka; 95%) and ~2.5 ka (SRD1; 1.7-3.6 ka; 95%). We have low confidence in these relations as they are secondary in nature. That is, liquefaction and strong ground shaking could relate to earthquake sources other than the Teton fault, and subsidence could occur as a result of gravitational failure of the Snake River delta.

### STEAMBOAT MOUNTAIN SITE

At the Steamboat Mountain site, movement of the east-dipping Teton fault has formed an uphill-facing scarp at the head of a prominent west-sloping alluvial-fan surface (Fig. 4a). Two geomorphic surfaces, which we interpret as fluvial terrace remnants related to the west-sloping alluvial fan, are preserved in the footwall of the fault. We infer that these surfaces signal fault movement and progressive footwall alluvial-fan surface uplift and abandonment (Fig. 4b), as they are bound on the east by the Teton fault. These surfaces postdate glacial retreat and are thus younger than ~15-14 ka—the time of widespread deglaciation in the region (Licciardi and Pierce, 2018). Surface 1 is about 2.0 m above the active stream channel (Fig. 4c); it continues laterally (downslope) about ~100-150 m west of the fault trace and has an eastern edge bounded by an ~0.5-m-high eastfacing fault scarp with 1.2 m of vertical separation (Fig 4c). Surface 2 is about 3.8-4.1 m above the modern channel and 1.8-2.1 m above surface 1 (Fig. 4c). Surface 2 is poorly preserved and has a lateral (downslope) extent of ~17 m west of the fault trace; its eastern edge is bounded by a 2.7 m high fault scarp with 3.3 m of vertical separation (Fig. 4c). The low topographic gradient directly adjacent to, and uphill from, the surface 1 and 2 scarps (Fig. 4b) signals alluvial sediments locally ponded against the scarps on the hanging wall of the Teton fault. Although axial streamflow along the fault north and south of our trench site (Fig. 4a,b) may have locally scoured and enhanced the fault scarp, we did not find evidence of stream erosion at the study site, where ponding has occurred. Trenches A and B extend across the ponded sediment onto surfaces 1 and 2, respectively.

We used hand tools to excavate two trenches across the normal-fault scarp at the Steamboat Mountain site (Figs. 4 and 5). Trench A completely crossed the 20.5-m-high (1.2-m-vertical-separation) fault scarp (Fig. 4c), had an orientation of  $\sim 070^{\circ}$ ,



Figure 5. Photographs of the Steamboat Mountain trench site. Upper panel shows trenches A (44.028692, -110.700819) and B (44.028472, -110.700711); view is to the south. Lower panel shows excavation of trench B using hand tools; view is to the west. Arrows mark approximate base of Teton fault scarp. Photos taken on 17 July 2017 by C. DuRoss. The color version of this figure is available only in the electronic edition.

and measured 8 m long, 1 m wide, and ≤2.1 m deep. Trench B was excavated about 20 m to the south of trench A (Fig. 5) and partly crossed the 2.7-m-high (3.3-m-vertical-separation) fault scarp (Fig. 4c). Trench B had an orientation of ~085° and measured 6 m long, 1 m wide, and ≤1.8 m deep. At each trench, we cleaned the trench walls and then photographed the exposures using a Canon EOS 70D camera with a 10-22 mm lens. We

constructed 0.5-mm-pixel photomosaics (Figs. 6 and 7) using Agisoft Metashape and the methods of Reitman et al. (2015). For horizontal and vertical control, we used 12-bit targets generated in Metashape and printed 25-50 cm apart on aluminum composite strips. Stratigraphic and structural relations (Figs. 6 and 7) were mapped in the field on acetate sheets overlying the printed photomosaics. Descriptions of stratigraphic units are included in the Appendix.

### Trench stratigraphy and structure

Trenches A and B exposed glaciofluvial, alluvial-fan, scarp-derived colluvial sediments (Figs. 6 and 7). Stratified coarse-grained glaciofluvial sediments in the footwall of the Teton fault are juxtaposed against finer-grained alluvialfan sediments and charcoal-rich paleosols (concentrated organic matter and charcoal fragments in soil A horizons) in the hanging wall. Sedimentary units displaced by the fault unconformably buried by poorly sorted scarp-derived colluvial sediments. These colluvial sediments bury paleosols formed in hanging-wall alluvial-fan units and have a laterally heterogeneous, coarse-tofine texture. We interpret a fault-scarp-derived origin for the colluvial sediments based on (1) their wedge-shaped geometries that reflect processes of scarp erosion and uncon-

formable deposition on the hanging wall, (2) slope-parallel clast fabric (e.g., stone lines) within the colluvium signaling local sediment transport and colluvial progradation, (3) alluvial-fan paleosols buried beneath the colluvial units that suggest rapid colluvial sedimentation, and (4) faults that terminate upward at the basal colluvial contacts. Further, we interpret the poorly sorted texture of the colluvium as reflecting processes of fault-

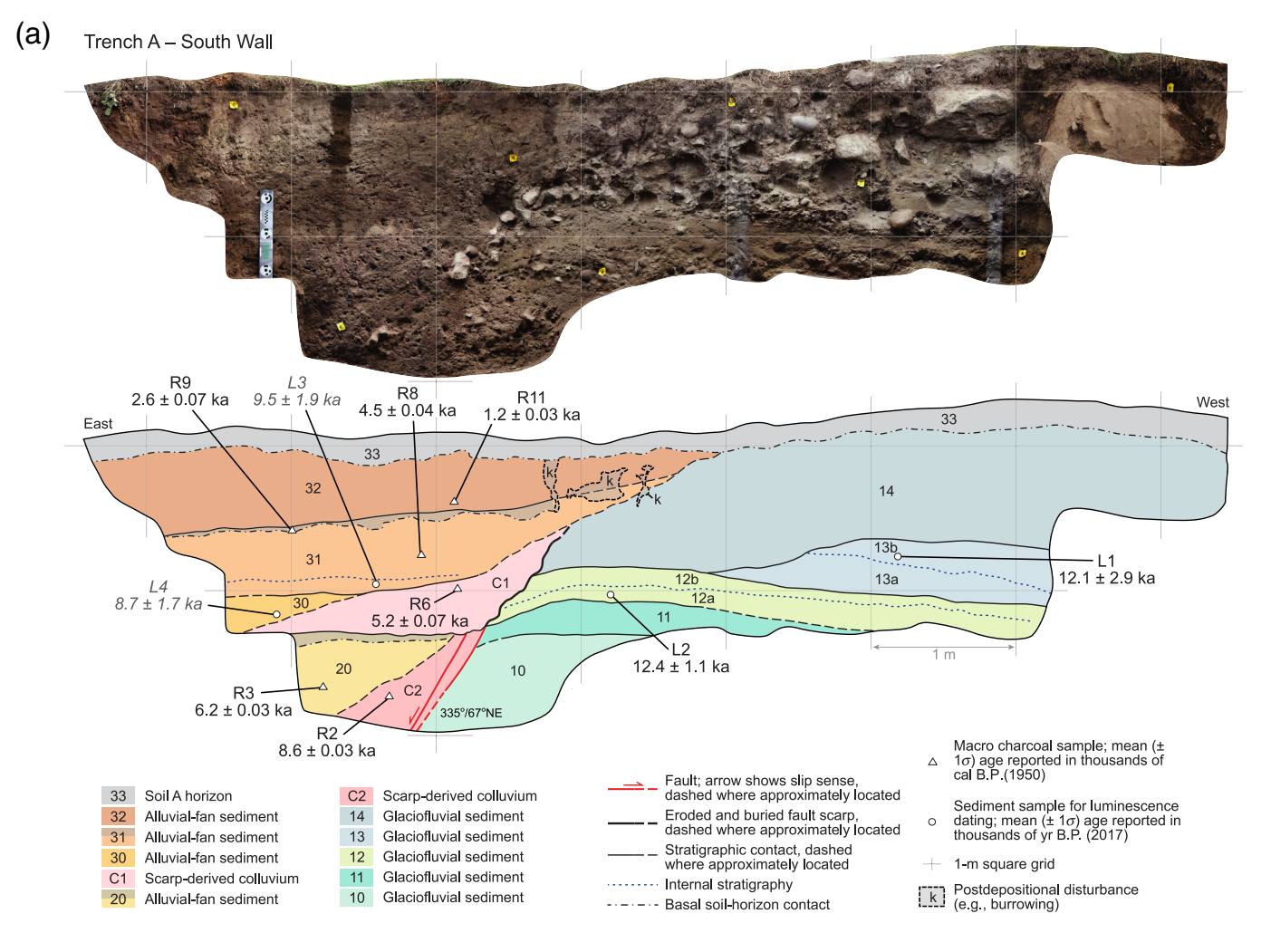


**Figure 6.** Stratigraphic and structural relations in (a) the south and (b) north walls of Steamboat Mountain trench A. Uninterpreted photomosaics were constructed using the methods of Reitman *et al.* (2015). Stratigraphic units are described in the Trench Stratigraphy and Structure section and the Appendix. Radiocarbon (<sup>14</sup>C) ages for charcoal and optically stimulated luminescence (OSL) ages for quartz sand are included in Tables 2 and 3,

respectively. Table 1 includes a summary of stratigraphic and structural evidence of surface-rupturing earthquake at the site. Ages excluded from Bayesian models are shown in italics. Vertical and horizontal grid lines are 1 m apart. The color version of this figure is available only in the electronic edition. (Continued)

scarp erosion and the colluvial deposition of coarse material on the hanging wall, combined with fine-grained alluvial-fan deposition and soil development. That is, the colluvial units are a mixture of both hanging-wall and footwall stratigraphic and pedogenic units. Alternative explanations for the colluvial units include storm-related sedimentation along the fault scarp or alluvial-fan deposition; however, these fail to reconcile our stratigraphic, structural, and pedogenic observations. Normal faults exposed in the trenches strike north-northwest (335°–349°) and dip 67°–83° east-northeast. In trench A, stratigraphic contacts in the footwall of the Teton fault (units 10–12) have evidence of fault drag or east-down warping within ~0.5 m of the fault zone (Fig. 6a).

Trench A exposed three packages of clastic sediment (Fig. 6): (1) glaciofluvial deposits (units 10–14) consisting of stratified sand, coarse gravel, cobbles, and  $\sim 1$  m diameter boulders in the fault footwall, (2) poorly sorted scarp-derived colluvium (units C1 and C2), and (3) relatively fine-grained alluvial-fan sediments (units 20 and 30–32), which locally include charcoal-rich paleosols. Units 10–14 likely have an ice-proximal glaciofluvial origin based on their well-defined stratification and local coarse texture, including cobble- and boulder-size clasts. Based on this texture, units 10–14 may represent sediments deposited by ice-fed streams in ice-marginal and morainal environments and were likely deposited at the site prior to or during deglaciation of the region. In contrast, the alluvial-fan sediments are consistently finer grained (dominantly silt to coarse sand) and have dispersed organic matter and paleosols. The scarp-derived colluvial sediments are fine grained, similar to the alluvial-fan sediments, but notably include gravel clasts,

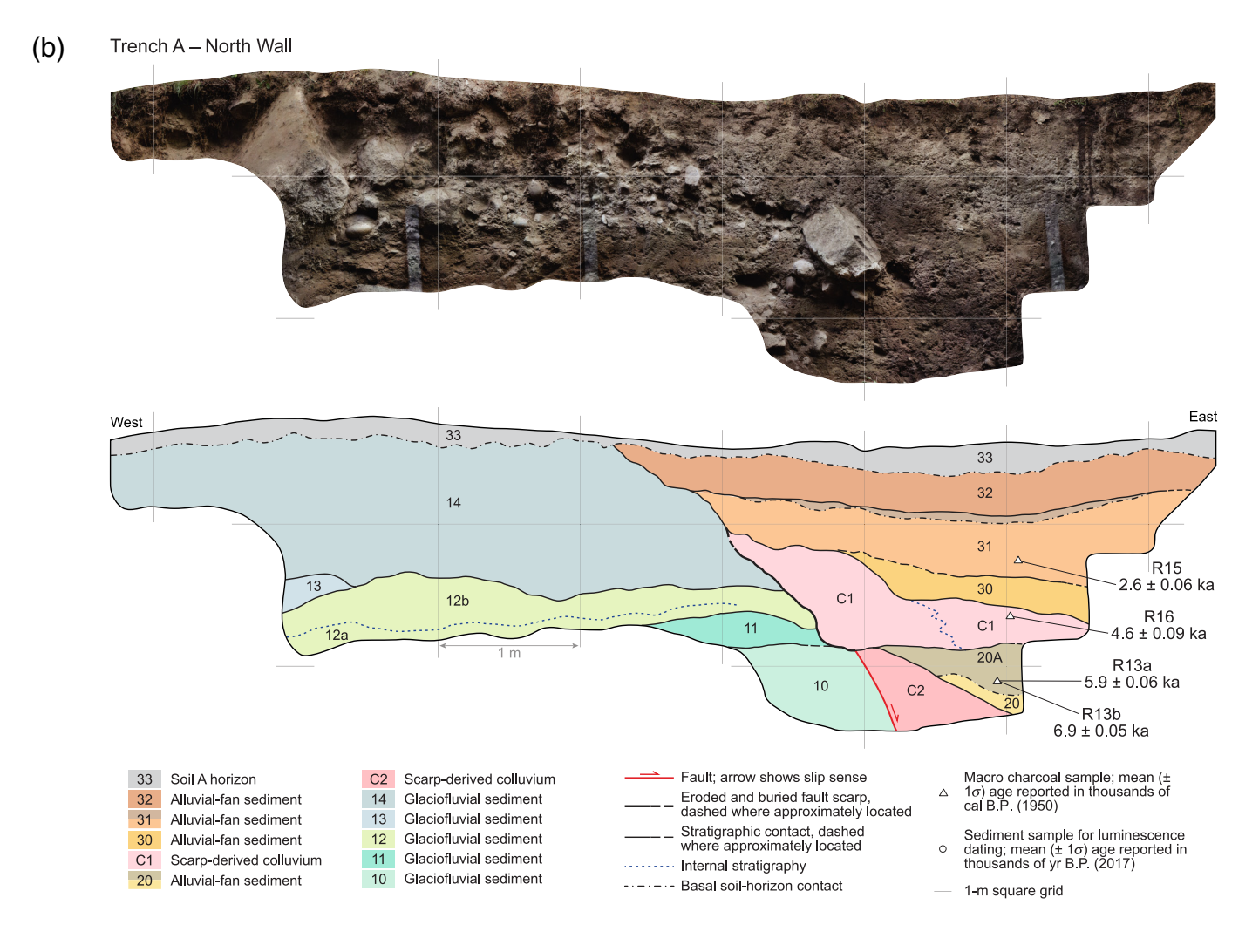


Figure 6. Continued

cobbles, and boulders that are likely eroded from footwall units 12–14.

Scarp-derived colluvial and alluvial-fan units in trench A have partially buried the Teton fault scarp and formed a buttress unconformity. For example, scarp-colluvial unit C1, as well as alluvial-fan units 31-32, unconformably overlie footwall units 12-14 (Fig. 6). We interpret this buttress unconformity, which lacks any evidence of shear, to represent an eroded uphill-facing scarp in glacially derived sediments (units 12-14) buried by at least 1.4 m of scarp colluvium and alluvial-fan sediments in the fault hanging wall. This amount of hanging-wall burial, if summed with the scarp height (0.5 m), yields a total scarp height (minimum vertical separation) of 1.9 m, nearly identical to the height difference of 2.0 m measured between surface 1 and the modern stream channel ~20 m to the north-northwest (Fig. 4b). We interpret the scarp height as only related to the SM1 rupture based on the geomorphology of the site and hanging-wall sedimentation rate ( $\sim$ 0.2-0.3 m/ka). That is, the SM2 scarp was

likely buttressed by at least a meter of hanging-wall sediments at the time of earthquake SM1. The relationship between scarp-colluvial unit C2 and overlying fan unit 20 (buttress unconformity) suggests a similar but older process of faulting, followed by hanging-wall burial (≥0.6 m). We did not expose the base of unit C2 in trench A and thus are unable to measure its thickness or estimate the height of the paleoscarp present prior to C2 deposition.

Trench B exposed three packages of clastic sediment (Fig. 7): (1) glaciofluvial deposits (unit 10) consisting of poorly sorted silt, sand, gravel, and cobbles in the fault hanging wall (unit 10a) and footwall (unit 10b), (2) poorly sorted deposits of scarp-derived colluvium (units C1 and C2), and (3) well-stratified alluvial-fan sediments (units 20–41) that locally include charcoal-rich paleosols (e.g., units 31, 33, and 41). Similar to that in trench A, stratification and coarse texture suggest that unit 10 may have a glaciofluvial origin. However, this unit is more poorly sorted and denser than units 10–14 in trench A and may represent subglacial deposits (e.g., subglacial till) rather than glaciofluvial

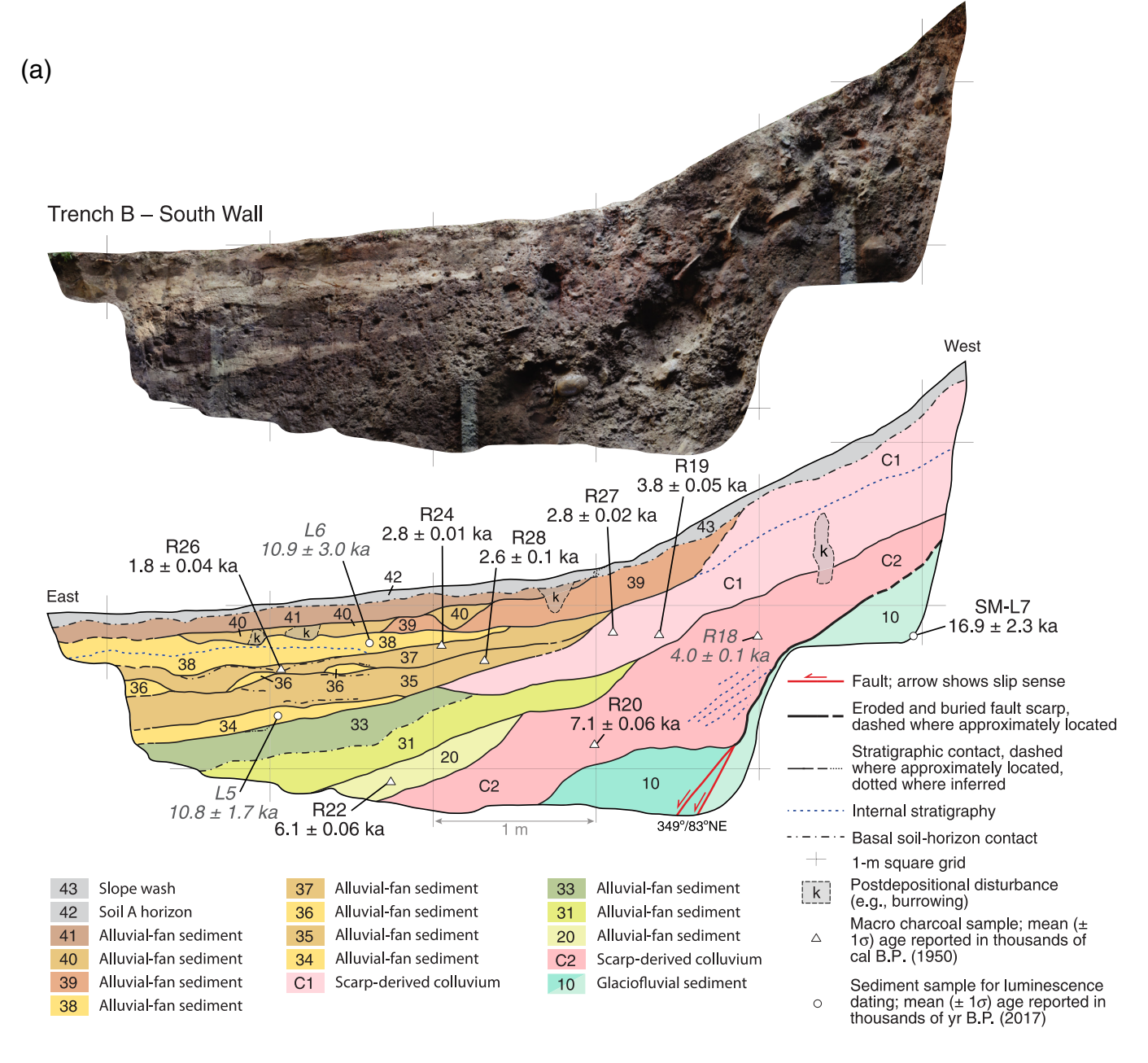


**Figure 7.** Stratigraphic and structural relations in (a) the south and (b) north walls of Steamboat Mountain trench B. Stratigraphic units are described in the Trench Stratigraphy and Structure section and the Appendix.

Radiocarbon (<sup>14</sup>C) ages for charcoal and OSL ages for quartz sand are included in Tables 2 and 3, respectively. Table 1 includes a summary of

stratigraphic and structural evidence of surface-rupturing earthquake at the site. Ages excluded from Bayesian models are shown in italics. Vertical and horizontal grid lines are 1 m apart. The color version of this figure is available only in the electronic edition. (*Continued*)

deposits. These units are coarser than the alluvial-fan units (dominantly silt-to-fine sand). The scarp-derived colluvial units are poorly sorted, have local slope-parallel clast fabric, and are interfingered with the westernmost parts of the alluvial-fan units. Unit 10 is faulted and unconformably overlain by scarp-colluvial unit C2. The lowermost fan sediments (units 20 and 31–32) and prominent paleosol (unit 33) postdate unit C2 and predate unit C1; whereas the uppermost fan units (units 34–41) and laterally

discontinuous paleosols postdate unit C1. Unit C1 is deposited conformably on C2 but is not exposed adjacent to a shear zone. Unit C1 likely continues and thickens to the west (into the fault scarp) and postdates faulting along an inferred fault to the west, not exposed in trench B.

Hanging-wall burial in trench B is similar to that in trench A. Alluvial-fan units 20-41 indicate a minimum of 1.3 m of hanging-wall burial, with  $\sim 0.6$  m postdating unit C2 and

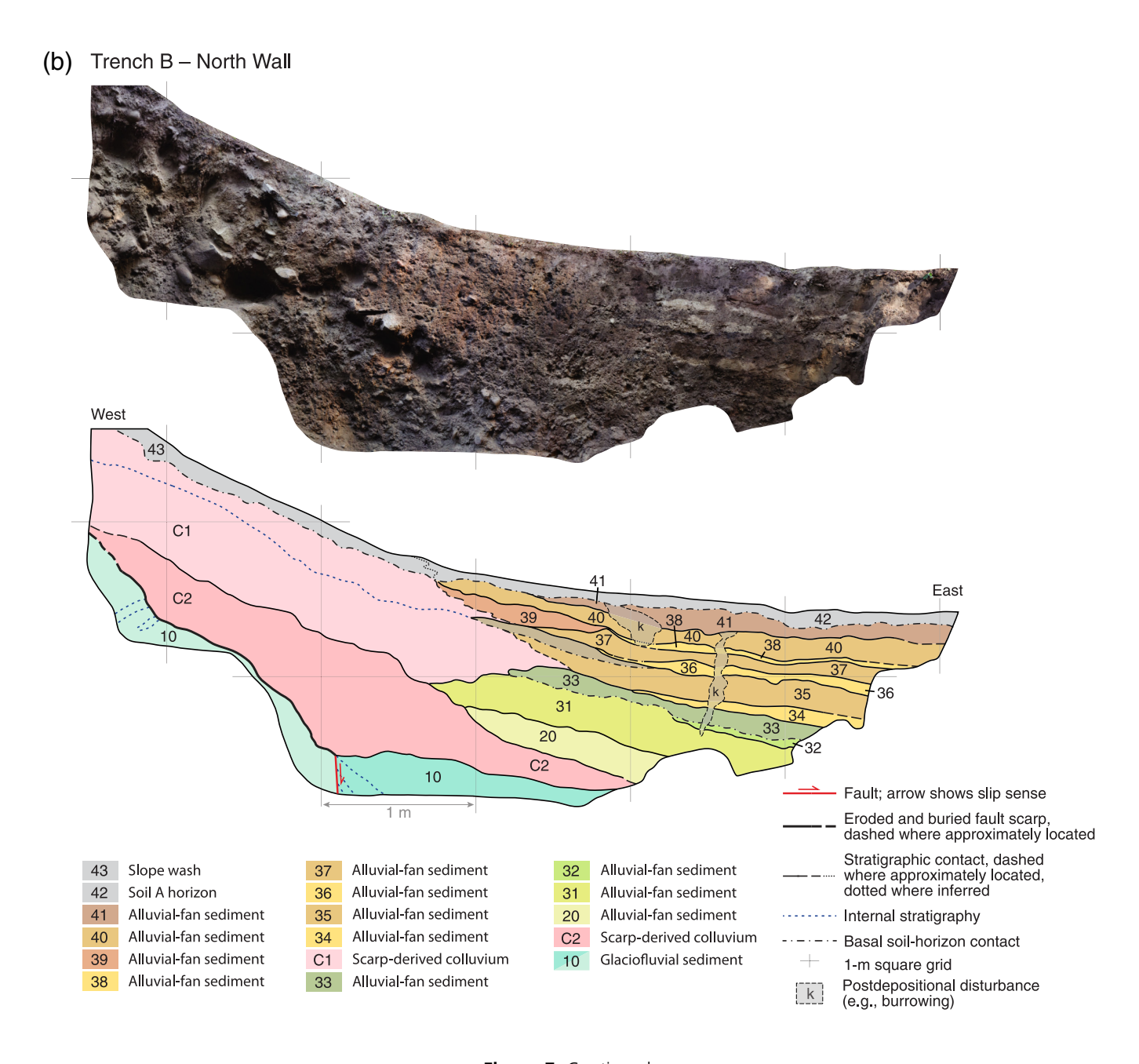


Figure 7. Continued

predating C1 and ~0.7 m postdating unit C1 (Fig. 7). Summing the amount of hanging-wall burial (1.3 m) with the scarp height (~2.7 m) yields a total scarp height of 4.0 m, identical to the height difference measured between surface 2 and the modern stream channel about 50 m to the north-northwest (Fig. 4b). Although the rate of hanging-wall deposition at trench B (~0.2 m/ka) is similar to that at trench A, the scarp height likely records displacement from two fault ruptures.

### **Evidence of surface rupture**

We summarize textural, stratigraphic, structural, and pedogenic evidence of surface-rupturing earthquakes in trenches A and B

(Table 1) following (DuRoss *et al.*, 2018). Together these data provide geologic evidence of at least two surface-rupturing earthquakes at the Steamboat Mountain site in postglacial time (<13–16 ka) and complement the geomorphic evidence for two ruptures based on scarps bounding surfaces 1 and 2.

Evidence of the penultimate rupture of the northern Teton fault is expressed in both trenches A and B. In trench A, scarp colluvial unit C2 has similar textural and stratigraphic evidence as that for unit C1 (see the Appendix). Poorly sorted and locally coarse sediment in unit C2 is faulted and overlain by finer grained, mostly flat-lying alluvial-fan sediments. We did not expose the base of unit C2 or any stratigraphic units beneath

TABLE 1
Summary of Stratigraphic and Structural Evidence of Surface-Rupturing Earthquakes

Trench, Event*	Textural Evidence	Stratigraphic/Geometric Evidence	Structural Evidence	Pedogenic Evidence	Summary of Event Evidence <sup>†</sup>
A, C2	Massive and poorly sorted silt, sand, and gravel with dispersed organic matter. Gravel clasts and cobbles are likely derived from unit 14.	Unit thickens away from fault trace and is unconformably overlain by westward-thinning alluvial-fan sediments. Geometry of exposed unit is similar to that for eastern part of unit C1.	Unit restricted to fault hanging wall; however, base of unit not exposed.	Underlying units not exposed; however, a well-expressed soil horizon in overlying unit 20 implies time prior to unit C1 deposition.	Moderate
A, C1	Massive and poorly sorted silt, sand, and gravel with dispersed organic matter. Gravel clasts and cobbles are likely derived from units 11–14.	Wedge-shaped geometry, with unconformable deposition on an eroded fault-scarp free face formed in units 11–14. Unconformably to conformably overlain by westward-thinning alluvial-fan sediments.	Unit restricted to fault hanging wall and overlies faulting in units 10–11 and C2.	Conformable deposition on paleosol formed within uppermost part of alluvial-unit 20.	Robust
В, С2	Moderately stratified silt and sand with gravel. Internal stratification consists of slope-parallel bedding within basal part of unit.	Wedge-shaped geometry, with unconformable deposition on glaciofluvial sediments (unit 10), including an eroded fault-scarp free face formed in unit 10. Conformably to unconformably overlain by westward-thinning alluvial-fan sediments.	Unit restricted to fault hanging wall and overlies fault zone formed in unit 10.	No paleosols exposed below unit; however, a well- expressed paleosol (unit 33), which implies time between C2 and C1 deposition.	Robust
B, C1	Weakly stratified, poorly sorted silt, sand, and gravel, with dispersed organic matter. Internal stratification consists of slope-parallel clast fabric.	Unit thickens into scarp; however, full extent of unit not exposed. Unit conformably overlies unit C2 but unconformably overlies units 31 and paleosol unit 33.	Unit likely restricted to fault hanging wall; however, causal fault zone not exposed.	Unit postdates well-expressed paleosol (unit 33), which implies time between C2 and C1 deposition.	Moderate

<sup>\*</sup>Units correspond to the Appendix.

it. Evidence of penultimate rupture in trench B includes a nearly completely exposed, wedge-shaped, and unfaulted scarp-derived colluvial unit (C2) that unconformably overlies faulted glaciofluvial sediments. Based on the moderate (~1-m) thickness of unit C2, its geometry that tapers sharply to the west at about the horizontal midpoint of the fault scarp, and its depth about 1 m below the surface (Fig. 7), we infer that unit C2 has buried a synthetic trace of the Teton fault, which was not reactivated in the youngest rupture at the site (additional discussion is included later). Unit C2 is buried by unit C1, which is texturally distinct from unit C2, thickens west into the fault scarp, and postdates hanging-wall alluvial-fan units 20 and 31–33 that bury the westernmost part of unit C2. These observations provide moderate-to-robust evidence of a penultimate earthquake rupture at the site (Table 1).

We exposed evidence of the most recent rupture in both the trenches. In trench A, a completely exposed, wedge-shaped, and unfaulted scarp-derived colluvial deposit (unit C1) overlies an eroded fault-scarp free face in glaciofluvial sediments and a paleosol in alluvial-fan sediments on the fault hanging wall. C1

postdates faulting and soil formation within the lower scarpcolluvial deposit C2. In trench B, unfaulted scarp-derived colluvium (unit C1) includes slope-parallel clast fabric and overlies a paleosol (unit 33) in alluvial-fan sediments on the fault hanging wall. Unit C1 thickens to the west, toward the fault scarp (Fig. 7), but was incompletely exposed by trench B, which only extended west to within  $\sim 2$  m of the scarp crest (Figs. 4c and 5). As a result, trench B did not expose a fault beneath unit C1, which complicates interpretations of the source of the colluvium. Unit C1 in trench B possibly represents a secondary pulse of colluvium, following a single surface-faulting earthquake. However, considering the textural differences between units C2 and C1 (see the Appendix) and the time between deposition of these units implied by alluvial-fan sedimentation (e.g., unit 20) and soil development (unit 33), we prefer the interpretation that unit C1 in trench B is evidence of a second surface-faulting earthquake. Further, the west-thickening geometry of C1 suggests that an additional structure to the west, beneath the ~2-m-wide unexposed part (uppermost ~one-half) of the fault scarp, is responsible for its formation.

<sup>†</sup>An overall assessment of the surface-rupture evidence ranges from moderate (most data support an earthquake origin) to robust (data overwhelmingly support an earthquake origin), following the criteria of (DuRoss et al., 2018).

TABLE 2 Charcoal Radiocarbon Ages for the Steamboat Mountain Trench Site

Sample Number*	Trench, Unit*	Sample Description <sup>†</sup>	Weight (mg)†	Lab Age ( <sup>14</sup> C yr B.P.)‡	Calibrated Age (cal B.P.)§	$\delta^{13}$ C (‰) $^{\parallel}$	Lab Number#
R2	A, C2	Pinus	2.7	7780 ± 30	8560 ± 30	-24.19	OS-139387
R3	A, 20	Pseudotsuga menziesii	12.8	$5435 \pm 25$	$6240 \pm 30$	-26.4	179164
R6	A, C1	Pinus	17.6	$4510 \pm 20$	$5160 \pm 70$	-23.9	179165
R8	A, 31	Populus	10.2	$4020 \pm 25$	$4480 \pm 40$	-25.5	179166
R9	A, 32	Pinus	15.4	$2495 \pm 25$	$2590 \pm 70$	-24.9	179167
R11	A, 32	Pinus	14.4	1265 ± 20	$1220 \pm 30$	-25.4	179168
R13a	A, 20	Pinus cone	9.8	$5140 \pm 30$	$5880 \pm 60$	-26.76	OS-139388
R13b	A, 20	Pseudotsuga menziesii	6.0	$6080 \pm 30$	$6940 \pm 50$	-22.72	OS-139389
R15	A, 31	Pinus	13.7	$2510 \pm 25$	$2600 \pm 70$	-25.3	179169
R16	A, C1	Abies	10.4	$4095 \pm 25$	$4630 \pm 90$	-24.6	179170
R18	B, C2	Pinus	3.9	$3650 \pm 20$	$3970 \pm 50$	-24.88	OS-139390
R19	B, C1	Pinus	14.9	$3530 \pm 20$	$3800 \pm 50$	-26.05	OS-139397
R20	B, C2	Populus	4.9	$6140 \pm 25$	$7050 \pm 60$	-22.67	OS-139398
R22	B, 20	Parenchymous tissue	1.4	$5340 \pm 20$	$6110 \pm 60$	-24.8	OS-139399
R24	B, 37/38	Pinus	14.5	$2620 \pm 20$	$2750 \pm 10$	-24.3	OS-139400
R26	B, 37/38	Pinus	28.5	1870 ± 15	$1810 \pm 40$	-24.31	OS-139401
R27	B, C1	Pinus	17.3	$2680 \pm 15$	$2780 \pm 20$	-23.78	OS-139402
R28	B, 35	Populus	5.4	2450 ± 15	$2550 \pm 100$	-25.49	OS-139403

<sup>\*</sup>Field sample numbers and units correspond to the Appendix. Samples in sequential order, but not included here (e.g., R4), were not submitted for radiocarbon dating.

The interpretation of units C1 and C2 related to separate earthquakes is also consistent with the evidence of two earthquakes in trench A. Together, these observations provide moderate-torobust evidence of the most recent earthquake rupture at the site (Table 1).

### **GEOCHRONOLOGY**

### Radiocarbon and luminescence dating

We submitted 18 samples for accelerator mass spectrometry radiocarbon dating (Table 2) and seven samples for quartz, single-aliquot optically stimulated luminescence (OSL) dating (Table 3). Samples for radiocarbon dating consisted of macro-charcoal fragments extracted from stratigraphic and pedogenic units. Following taxonomic identification (Table 2), we selected the shortest-lived plant genera or species for dating. We used OxCal (Bronk Ramsey, 2009) to calibrate the radiocarbon ages, which are reported in calendar years before 1950 Common Era (C.E.) and rounded to the nearest decade. Samples for OSL dating consisted of fine-grained (90–125  $\mu$ m) clastic sediment extracted from the trench walls using opaque tubes (following the methods of Gray et al., 2015). OSL ages were calculated using central and minimum age models (e.g., Galbraith, 2010); ages are reported in calendar years before 2017 C.E., rounded to the nearest decade. The resulting radiocarbon and OSL ages provide geochronological control for stratigraphic and pedogenic units exposed in the trenches.

Radiocarbon and OSL ages provide geochronological context for pre-faulting (e.g., glaciofluvial) and post-faulting (e.g., scarp-colluvial and alluvial-fan) depositional events (Tables 2 and 3). These ages suggest that the two Teton fault surface ruptures recorded at the Steamboat Mountain site occurred after deposition of glaciofluvial sediments in the footwall at ~12 ka and before deposition of scarp-colluvial (unit C1) and alluvialfan sediments in the hanging wall at  $\sim$ 2–5 ka. Constraints on the depositional events and surface ruptures are discussed later and provide a framework for Bayesian modeling of earthquake timing at the site.

Glaciofluvial sediments at the site (units 10-14) predate the penultimate and the most recent earthquake ruptures and are constrained to ~12.1–12.4 ka in trench A (L1 and L2) and possibly  $\sim$ 16.9 ka in trench B (L7). The penultimate rupture postdates these ages and is constrained by radiocarbon ages from trench A to a minimum of ~5.9-6.9 ka (unit 20; R3, R13a-b) and possibly ~8.6 ka (unit C2; R2). In trench B, minimum ages for the penultimate rupture of  $\sim$ 6.1 ka (R22) and  $\sim$ 7.1 ka (R20) from units 20 and C2, respectively, are most consistent with the trench A ages. The most recent earthquake postdates these unit C2 ages and is constrained to a minimum of ~4.6-5.2 ka in trench A (R16, R6) and ~2.8-3.8 ka in trench B (R27, R19) using radiocarbon ages for scarp-colluvial unit C1. Alluvial-fan sediments and pedogenic horizons postdating unit C1 (e.g., trench A units 30-32; trench B units 35-38) are dated to

<sup>&</sup>lt;sup>†</sup>Charcoal taxonomy and weight by PaleoResearch Institute, Golden, Colorado.

 $<sup>^{\</sup>ddagger}$ Laboratory age reported in radiocarbon years before present (1950); error is one standard deviation (1 $\sigma$ ) of analytical uncertainty.

 $<sup>^{\</sup>S}$ Calendar calibrated age reported as mean and  $1\sigma$  uncertainty, rounded to the nearest decade. Calculated using OxCal v.4.3 (Bronk Ramsey, 2009).

<sup>&</sup>lt;sup>II</sup>Delta <sup>13</sup>C, measured on a split of sample.

<sup>\*</sup>Laboratory identifier. Numbers preceded by "OS-" (e.g., OS-139387) were processed at the Woods Hole Oceanographic Institution, National Ocean Sciences Accelerator Mass Spectrometry facility. All others (e.g., 179164) were processed at the Lawrence Livermore National Laboratory, Center for Accelerator Mass Spectrometry.

Stimulated Luminescence Ages for the Steamboat Mountain Trench Site Optically FABLE 3

Sample Number*	Trench, Unit*	Water Content (%)⁺	¥(%) ¥	±(mdd) U	Th (ppm)‡	Cosmic Dose (Gy/ka)§	Total Dose Rate (Gy/ka)	Equivalent Dose (Gy)	2	Scatter#	CAM Age (ka)**	MAM Age (ka)**
11	A, 13	11 (42)	$2.84 \pm 0.13$	$3.09 \pm 0.25$	$12.84 \pm 0.43$	$0.003 \pm 0.001$	$4.01 \pm 0.11$	$48.7 \pm 5.6$	11 (42)	44	$21.2 \pm 3.5$	$12.1 \pm 2.9$
7	A, 12	14 (40)	$2.7 \pm 0.04$	$2.66 \pm 0.09$	$10.54 \pm 0.12$	$0.003 \pm 0.001$	$3.53 \pm 0.05$	$43.9 \pm 2.1$	14 (40)	12	$12.4 \pm 0.8$	$12.4 \pm 1.1$
[]	A, 31	19 (67)	$2.85 \pm 0.09$	$3.36 \pm 0.18$	$12.22 \pm 0.31$	$0.003 \pm 0.001$	$3.72 \pm 0.08$	$35.5 \pm 3.8$	19 (67)	34	$13.5 \pm 1.6$	$9.5 \pm 1.9$
47	A, 30	16 (56)	$2.7 \pm 0.05$	$2.92 \pm 0.1$	$10.56 \pm 0.15$	$0.002 \pm 0.001$	$3.51 \pm 0.05$	$30.7 \pm 3.3$	16 (56)	32	$12.1 \pm 1.1$	$8.7 \pm 1.7$
L5	B, 34	18 (49)	$3.09 \pm 0.04$	$3.35 \pm 0.09$	$11.2 \pm 0.13$	$0.007 \pm 0.001$	$3.89 \pm 0.05$	$42.1 \pm 3.3$	18 (49)	27	$11.7 \pm 1.0$	$10.8 \pm 1.7$
97	B, 38	12 (55)	$3.29 \pm 0.08$	$3.39 \pm 0.15$	$13.8 \pm 0.28$	$0.023 \pm 0.002$	$4.5 \pm 0.08$	$49.1 \pm 6.0$	12 (55)	24	$12.8 \pm 1.7$	$10.9 \pm 3.0$
77	B, 10	7 (29)	$3.14 \pm 0.04$	$3 \pm 0.09$	$13.8 \pm 0.16$	$0.002 \pm 0.001$	$4.51 \pm 0.05$	$76.0 \pm 4.5$	7 (29)	16	$16.9 \pm 1.5$	$16.9 \pm 2.3$

correspond to the Appendix. Samples processed by the U.S. Geological Survey Luminescence Dating Laboratory, Denver, Colorado Field moisture percentage based on weight; complete sample saturation percent in parentheses Field sample numbers and units

Background radiation for bulk sediment from the sample location. Analyses obtained using laboratory gamma spectrometry (high-resolution germanium detector) or inductively coupled plasma mass spectrometry. Cosmic doses and attenuation with depth ~1.6-4.5 ka in trench A (R11, R9, R15, R8) and ~1.8-2.8 ka in trench B (R26, R28, R24). OSL ages (applying a minimum age model; Table 3) provide considerably older minimum ages for the post-unit C1 alluvial-fan units of ~8.7-9.5 ka in trench A (L3, L4) and 10.8-10.9 ka in trench B (L5, L6). Notably, these OSL ages are thousands of years older than radiocarbon ages from stratigraphically similar sample locations (e.g., 4.5 ka-R8 versus 9.5 ka-L3 for unit 31; trench A). These differences are not well understood, but could signal partially bleached sediment related to (1) a short depositional travel path of sand grains in the relatively limited alluvial-fan drainage network upslope of the trench site, (2) turbid water related to post-fire debris flows, and/or (3) the reworking of glacial deposits (e.g., subglacier sediment and moraines) having an inherited age component. In addition, volcanic bedrock could provide source material for sediment at the site and, thus, yield poorly bleached OSL results owing to sand grains that have not experienced multiple depositional cycles and have low OSL sensitivity (Rhodes, 2011).

### **Bayesian modeling**

We developed a single Bayesian prior (stratigraphic) model for the Steamboat Mountain site (Fig. 8) that takes into account depositional unit ordering information, crosscutting relations, and the similar exposure of glaciofluvial, scarp-derived colluvial, and alluvial-fan sediments in trenches A and B. In this model, earthquakes SM2 and SM1 postdate glacial and postglacial units 10, 12, and 13 constrained to ~12-16 ka. As trenches A and B are only ~20 m apart on the same scarp, we consider it most likely that the evidence of two ruptures in each trench is related to only two earthquakes at the site. Units C2 and 20 postdate earthquake SM2, predate SM1, and are constrained to ~5.9-6.9 ka. Deposition after SM1 consists of scarp-derived colluvium (unit C1) between ~2.8 and 5.2 ka, and a more recent period of alluvial-fan deposition on the fault hanging wall between ~1.2 and 2.7 ka. These sedimentary units describe a nearly continuous sequence of deposition at the site, especially from  $\sim$ 9 to  $\sim$ 1-2 ka. We expect that the depositional record, and possibly the site earthquake history, is incomplete between the postglacial units and unit C2. In trench A, an incomplete record likely relates to the limited exposure of unit C2 and the lack of exposure of any hanging-wall alluvial-fan units predating unit C2. Trench B yielded a more complete exposure of unit C2, but the lack of alluvialfan units or soils postdating the glacial units and predating C2 suggests a depositional hiatus.

Of the 25 total radiocarbon and OSL ages, we used 19 to constrain the Bayesian likelihood (geochronologic) model. These ages include three OSL ages (L1, L2, and L7) that constrain the glacial and postglacial units. We excluded four additional OSL ages (L3–L6) for younger alluvial-fan and colluvial units because they are between 4 and 9 ka older than radiocarbon ages from similar stratigraphic positions (e.g., the ~10.9 ka age for L6 compared with the 1.8–2.8 ka ages for

equivalent dose. Numbers in parentheses indicate total number of measurements included in calculating the represented equivalent dose. equivalent dose values; values >30% are considered to be poorly bleached of replicated equivalent dose estimates used to calculate the final overall

µm quartz grains using a central age model (CAM) and minimum age model (MAM). Ages reported in thousands of years before sample processing date (2017), calculated field moisture values,

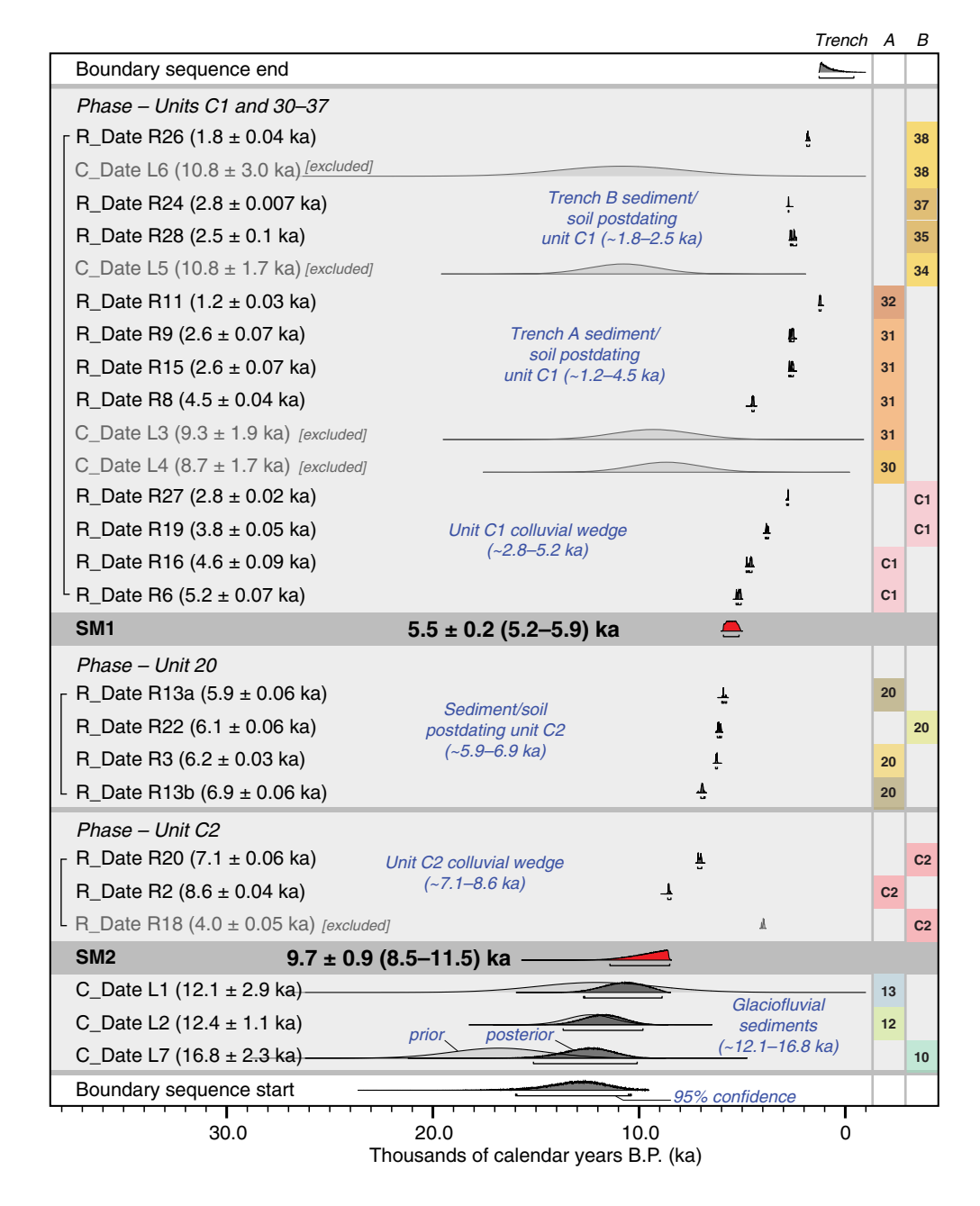


**Figure 8.** Bayesian (OxCal) model for the Steamboat mountain site, showing stratigraphic ordering information and geochronologic data from trenches A and B that constrain Steamboat Mountain earthquakes SM2 and SM1. Earthquake SM2 postdates latest Pleistocene glacial/postglacial sediments and is broadly constrained to  $\sim$ 8.5–11.5 ka. Earthquake SM1 occurred within a period of hanging-wall alluvial fan sedimentation and is constrained to  $\sim$ 5.2–5.9 ka. Mean earthquake ages with 1 $\sigma$  uncertainty and 95% confidence bounds in parentheses are reported. Ages for radiocarbon samples (e.g., R2; 7780, 30) are uncalibrated laboratory <sup>14</sup>C ages with 1 $\sigma$  uncertainty. The color version of this figure is available only in the electronic edition.

R24 and R26; Fig. 7a). We have greater confidence in the radiocarbon ages for these deposits, which yield a consistent stratigraphic age progression (Fig. 8). We only exclude a single radiocarbon age (~4.0 ka, R18), which is several thousand years younger than an additional age for trench B unit C2 (~7.1 ka, R20), is stratigraphically inconsistent with unit 20 (~6.1 ka, R22) (Fig. 7a), and likely represents reworked organic matter. Excluding R18 yields a broader time distribution for earthquake SM1.

## Earthquake timing and displacement

Our Bayesian model constrains the timing of Steamboat Mountain earthquakes SM2 and SM1 (Fig. 8). Earthquake SM2 postdates deposition of postglacial sediments with ages as late as  $\sim 12.1-12.4$  ka (L1, L2) and predates deposition of unit C2 at ~7.1-8.6 ka (R2, R20). The SM2 probability distribution function (PDF) yields a mean of  $9.7 \pm 0.9$  ka  $(1\sigma)$  and 95% confidence bounds of 8.5-11.5 ka. The SM2 PDF is broadly constrained with an asymmetric shape that is skewed toward ~8 ka; this shape reflects a broadly constrained maximum age (L1,  $12.1 \pm 2.9$  ka) for SM2 and a tightly constrained minimum limiting age (R2,  $8.6 \pm 0.04$  ka). Earthquake SM1 occurred within a welldated sequence of alluvial-fan and colluvial deposition on the hanging wall. Alluvial-fan deposition prior to SM1 occurred as late as 5.1 ka (R13) and scarp-derived colluvium in unit C1 is as old as 4.5 ka (R6). These constraints yield a mostly symmetrical constrained narrowly earthquake SM1 PDF, which has a mean of  $5.5 \pm 0.2$  ka  $(1\sigma)$  and 95% confidence 5.2-5.9 bounds of Additional ages for C1 as well

as alluvial-fan deposits that are stratigraphically above C1 are between 3.8 ka (R19) and 1.2 ka (R11) and generate confidence in the mid-Holocene result for SM1.

We use the thickness of hanging-wall sediments, scarp height, and the vertical displacement of surfaces across the Teton fault to estimate displacement for earthquakes SM2

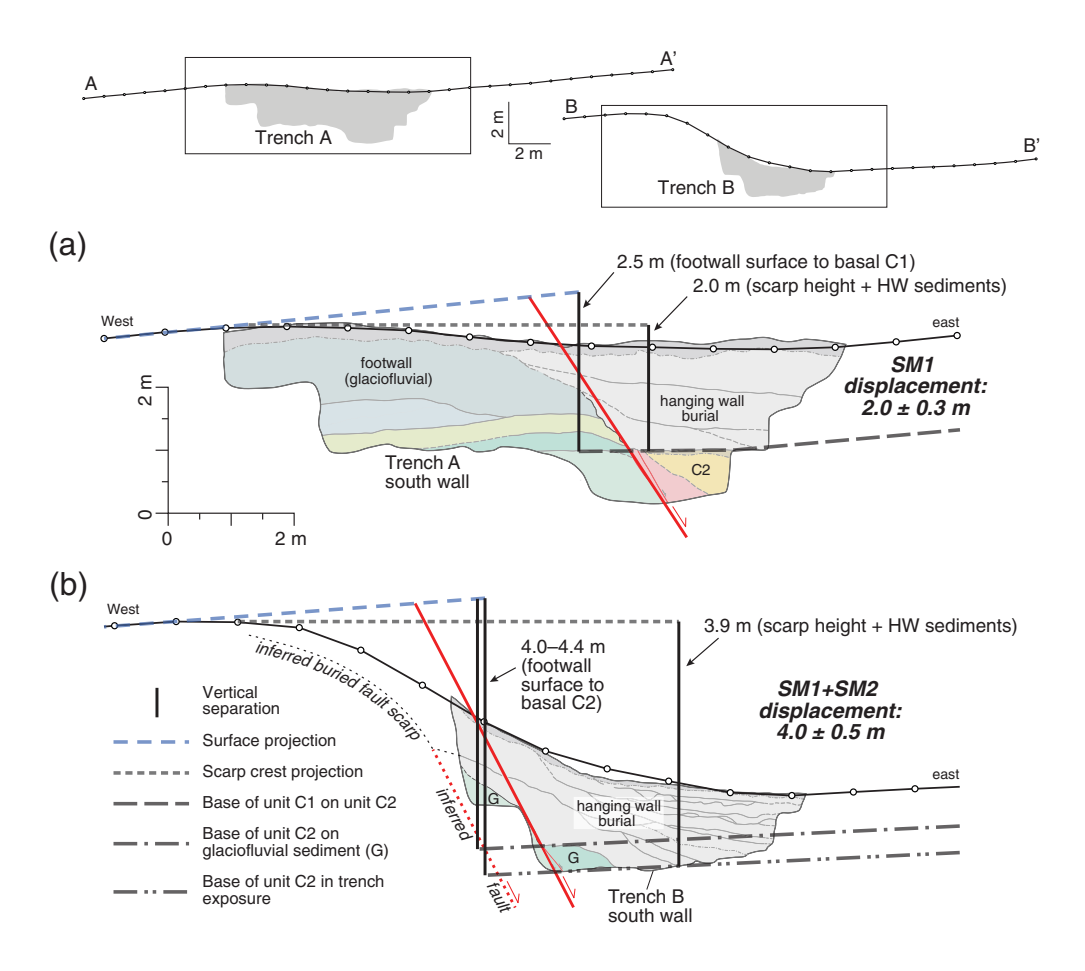


**Figure 9.** Vertical displacement at the Steamboat Mountain site, calculated using topographic profiles (Fig. 4c), scarp height, fault geometry, and the thickness of hanging-wall sediments exposed in trenches A and B. (a) Excerpt of topographic profile A–A', showing trench A and vertical-displacement estimates of 2.0–2.5 m, based on the surface geometry, scarp crest (short-dashed line), and base of unit C1 scarp-derived colluvium (long dashed line). Our preferred vertical displacement for SM1 of  $2.0 \pm 0.3$  m ( $\sim 1\sigma$ ) accounts for these measurements as well as a minimum displacement estimate of 1.3 m based on post-C2 hanging-wall (HW) stratigraphy. (b) Excerpt of topographic profile B–B', showing trench B and vertical-displacement estimates of 3.9–4.4 m based on the surface geometry, scarp crest, and base of scarp-derived colluvial and HW deposits (dashed-dotted lines). An unexposed fault and buried fault scarp are inferred west of the trench B based on colluvial stratigraphy (see the Evidence of Surface Rupture section for discussion) but do not affect the displacement measurements. Our preferred total vertical displacement for earthquakes SM1 and SM2, based on these measurements, is  $4.0 \pm 0.5$  m. The color version of this figure is available only in the electronic edition.

and SM1 in trench A. Hanging-wall sediments that postdate units C2 and 20 are 1.4 m thick and provide a minimum estimate of vertical displacement in earthquake SM1. We measured 2.5 m of vertical displacement for SM1 by projecting the west-sloping footwall surface (Fig. 4c) and subhorizontal alluvial-fan surface (unit 20) in the hanging wall into the fault zone (Fig. 9a). However, because of the potential for the west-sloping surface to overestimate the vertical separation, we also measure 2.0 m of vertical separation between the pre-C1 pale-osurface (top of unit C2) and the scarp crest (Fig. 9a). These reconstructions assume that the 0.5 m high scarp only records displacement in SM1. If both SM1 and SM2 are recorded in the surface scarp, then our SM1 displacement may be

overestimated. Conversely, the subhorizontal orientation of the hanging-wall surface, compared with the west-sloping footwall, could signal fault drag (east-down rotation of the hanging wall adjacent to the fault zone). Drag is apparent in the contacts between glaciofluvial units in the trench A footwall; if similar occurred on the hanging wall, then our estimate of SM1 vertical displacement could be understated. Finally, the presence of an unexposed antithetic fault east of our trench would also serve to reduce our vertical displacement measurement. However, although antithetic faulting and graben formation is possible based on the local-scale geomorphology of the fault (Fig. 4a), we did not interpret graben formation at the site scale (Fig. 4b). Considering these factors, as well as the limited extent of the exposure, we estimate  $2.0 \pm 0.3$  m ( $\sim 1\sigma$ ) of vertical displacement in SM1. The displacement for SM2 in trench A poorly constrained >0.6 m, due to the limited exposure of unit C2. However, considering the similar shapes and geometries of units C2 and C1, and the degree of burial by overlying fan units 20 and 30-31, it is plausible that SM2 had a similar amount of displacement as

that SM2 had a similar SM1 ( $\sim$ 2 m).

We estimate vertical displacements for SM1 and SM2 at trench B using the footwall (surface 2) and hanging-wall surface geometry (Fig. 4c) as well as the thickness of hanging-wall deposits observed in the trench (Fig. 7). We measure 4.0–4.4 m of vertical separation using the west slope of surface 2 (Fig. 4c) and the basal contact of scarp-derived colluvial sediments projected into the fault zone with a slope identical to that on the hanging-wall surface (Fig. 9b). The range in displacement reflects projections based on the base of C2 on glaciofluvial unit 10 (4.0 m) and the base of unit C2 in the exposure (4.4 m) (Fig. 9b). Similar to that in trench A, we also use the scarp crest to measure displacement.

This combination of scarp height and thickness of hanging-wall sediments yields an approximate vertical displacement of 3.9 m. Our estimate of 3.2–3.4 m of vertical separation across the scarp (Fig. 4c) serves as a minimum displacement for SM1 and SM2 as the hanging-wall includes deposits that postdate units C2 and/ or C1. Similar to that for trench A, we cannot rule out antithetic faulting outside of the extent of trench B, which, if present, would serve to decrease per-event displacement. Considering our scarpheight and displacement measurements, we estimate a total of  $4.0 \pm 0.5$  m ( $\sim 1\sigma$ ) of vertical displacement for earthquakes SM1 and SM2. Hanging-wall sediments appear equally apportioned to earthquakes SM2 (~0.6 m post C2) and SM1 (~0.7 m post C1); thus, we divide the total displacement equally between the two earthquakes. We estimate an average of  $2.0 \pm 0.5$  m  $(\sim 1\sigma)$  each for SM2 and SM1; the uncertainty estimate reflects the incomplete exposure of the fault zone and pre-SM2 hangingwall surface.

We integrate observations from trenches A and B and estimate vertical displacements of 2.0  $\pm$  0.6 m in earthquake SM1 and 2.0  $\pm$  1.0 m in SM2 at the Steamboat Mountain site. The uncertainty for SM1 reflects the propagation of SM1 displacement uncertainties (0.3 and 0.5 m) in quadrature (square root of the sum of the squares). SM2 may have had a similar displacement based on the similar styles and amounts of hanging-wall deposition in trenches A and B and the heights of fluvial terraces 1 and 2 (profile C-C'; Fig. 4c), but we have less confidence in this estimate because we are unable to accurately measure SM2 displacement in trench A. As a result, we estimate  $2.0 \pm 1.0$  m of vertical displacement in SM2. Our uncertainty estimate reflects our incomplete knowledge of SM2 displacement in trench A (estimated at  $2.0 \pm 0.9$  m and propagated in quadrature with trench B uncertainty of 0.5 m). Importantly, the SM1 and SM2 displacement uncertainties are correlated, where greater displacement in one of the earthquakes would require less displacement in the other to conserve the cumulative displacement of  $\sim$ 4 m at the site. However, the SM1 and SM2 displacement estimates correspond with the progressively uplifted footwall fluvial surfaces (~2 and ~4 m above local stream incision; Fig. 4c), which lend confidence to our results.

### **DISCUSSION**

### Paleoseismology of the Steamboat Mountain site

The depositional and tectonic sequence of events at Steamboat Mountain includes at least two postglacial surface-faulting earthquakes. During the most recent glaciation of the Yellowstone plateau (~13-16 ka), the Snake River ice lobe flowed south toward Jackson Hole, creating subglacially sculpted topography at the site, now occupied by the Snake River to the west and Jackson Lake to the south (Pierce et al., 2018). The Snake River terminal moraine is dated to  $15.5 \pm 0.5$  ka near Leigh Lake, which yields a maximum constraint on widespread deglaciation of the region at ~14-15 ka (Licciardi and Pierce, 2018).

Following deglaciation, degradation of glacial landforms and unconsolidated deposits likely occurred, resulting in the deposition of glaciofluvial sediments. At Steamboat Mountain, glaciofluvial sediments are as young as ~12 ka. Following glaciofluvial deposition, earthquake SM2 occurred at 9.7 ka (8.5-11.5 ka; 95%) on the Teton fault, with 2.0  $\pm$  1.0 m of down-to-the-east vertical displacement. Scarp-derived colluvial and alluvial-fan sedimentation occurred on the hanging wall between ~8.6 and 5.9 ka, postdating earthquake SM2. Earthquake SM1 ruptured the site at 5.5 ka (5.2-5.9 ka; 95%), with 2.0  $\pm$  0.6 m of vertical displacement. Hanging-wall sedimentation following SM1 occurred between ~5.2 and 1.2 ka.

Earthquake SM1 is well constrained to 5.2-5.9 ka at 95% confidence, which reflects the high fidelity of the Steamboat Mountain paleoseismic stratigraphy and chronology. First, the record consists of fine-grained, organic-rich alluvial-fan sediments that have partially buried the hanging wall. Although charcoal from these units is mostly detrital, the 12  $^{14}\mathrm{C}$  ages from the alluvial-fan sediments are stratigraphically consistent, suggesting they are not heavily skewed by an inherited age component (e.g., >500 yr; Nelson, 1992; DuRoss et al., 2018). This could be consistent with frequent, prehistoric forest fires in the region (~50-200 yr recurrence; Houston, 1973; Loope and Gruell, 1973; Millspaugh and Whitlock, 1995) and rapid post-fire deposition at the site. Fire-related and likely turbid fan deposition could explain the anomalously old (poorly bleached) OSL ages for the hanging-wall units. In trench A, alluvial-fan sediments that bury the scarp-derived colluvial units have served to diminish scarp erosion and colluvial deposition. This has resulted in a reduction of associated recycling of organic matter from the footwall (e.g., DuRoss et al., 2018) and, thus, stratigraphically consistent ages for the hanging-wall units. In trench B, fan sediments are interbedded with the colluvial units and provide additional constraints on the timing of deposition. Finally, because of the fine-grained nature of the sediments, post-depositional disturbance was clear. Together, these factors yield a highly reliable terrestrial paleoseismic record.

Based on the geomorphology of the Steamboat Mountain site and the sedimentary record exposed, we infer that the earthquake history of the site is complete since about 9-11 ka. Geomorphic mapping demonstrates that only a single postglacial fault trace is present at the latitude of the site (Fig. 2a). Although sedimentation related to Jackson Lake has locally obscured the surface geomorphology, light detection and ranging (lidar) data from east and west of the Snake River floodplain and northernmost arm of Jackson Lake do not show evidence of throughgoing structures crossing the lake or Snake River valley to the north of the site (Zellman, DuRoss, and Thackray, 2019). Further, we did not observe evidence of stream erosion at our site, which has low topographic relief and has trapped alluvialfan sediments on the downthrown (eastern) side of the Teton fault. Our trench exposures support this; we observed onlapping

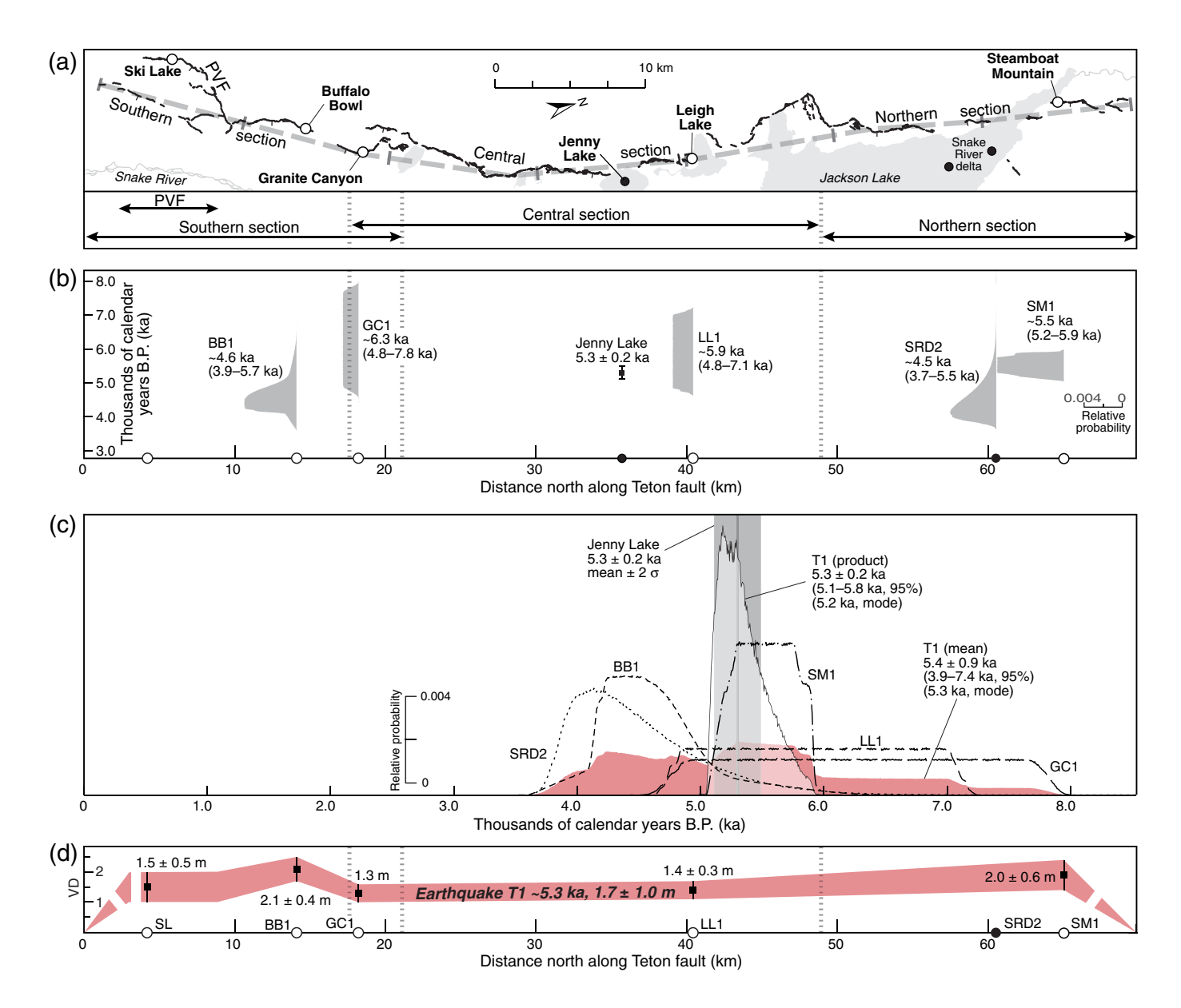


**Figure 10.** Timing and rupture extent of the youngest Teton fault surface-faulting earthquake (T1). (a)  $\sim$ 70 km long surface trace of the Teton fault from Zellman, DuRoss, and Thackray (2019); heavy dashed line shows simplified trace from DuRoss *et al.* (2019). Arrows and dotted lines in lower panel show extent of fault sections and the Phillips Valley fault (PVF). (b) Earthquake-timing probability density functions (PDFs) along the Teton fault for the youngest earthquakes identified at paleoseismic trench sites (Byrd, 1995; DuRoss *et al.*, 2019; Zellman, DuRoss, Thackray, *et al.*, 2019). SRD2 is the penultimate earthquake inferred from geomorphic relations along the lower Snake River delta (Pierce *et al.* (1998); the SRD2 PDF is from DuRoss *et al.* (2019). The Jenny Lake  $\sim$ 5.3  $\pm$  0.2 ka (2 $\sigma$ ) disturbance

horizon is from Larsen *et al.* (2019). Dotted lines show section boundaries. (c) Comparison of earthquake-timing PDFs. T1 (mean) PDF is bin-wise mean of overlapping PDFs BB1, GC1, LL1, SRD2, and SM1; T1 (product) PDF is bin-wise product of these PDFs. Jenny Lake  $\sim$ 5.3 ka disturbance horizon is shown as vertical bar for comparison. (d) Possible surface-rupture extent and distribution of vertical displacement (VD). Mean displacement for T1 of  $\sim$ 1.7  $\pm$  1.0 ( $\sim$ 1 $\sigma$ ) m is based on BB1, GC1, LL1, SRD2, SM1, and the Ski Lake (SL) site. Along-strike displacement at fault ends is poorly constrained and assumes a linear taper to southern and northern fault termini. Rupture length is 51 km between BB1 and SM1 or 70 km along the entire fault. The color version of this figure is available only in the electronic edition.

alluvial-fan strata, rather than erosional channels (e.g., defined by concave-up basal geometries). The timespan over which the site record is likely complete is from the stratigraphically intact and well-dated record of hanging-wall sedimentation that post-dates earthquake SM2 (Fig. 8). In contrast, the period between glaciofluvial sedimentation at the site and earthquake SM2 could

be incomplete as we did not fully expose the glaciofluvial sediments on the hanging wall of the fault in trench A or along a likely western strand in trench B. Using these factors, we infer that the Steamboat Mountain site yields a complete record of surface-faulting earthquakes on the northern Teton fault since the early Holocene (~9–11 ka).

## Timing and spatial extent of the youngest Teton fault rupture

**Synthesis of Teton fault terrestrial earthquake records.** Terrestrial paleoseismic records indicate that at least three earthquakes ruptured the Teton fault during the early-to-middle Holocene (~4–11 ka) (Byrd, 1995; DuRoss *et al.*, 2019; Zellman, DuRoss, Thackray, *et al.*, 2019). Here, we compare the Steamboat Mountain record with these previous paleoseismic data and evaluate the timing of the youngest rupture of the Teton fault by quantitatively combining earthquake-timing PDFs derived from these sites.

Earthquakes SM2 and SM1 correspond with earthquakes identified in previous paleoseismic investigations (Fig. 10a,b). Earthquake SM2 (8.5–11.5 ka; 95%) overlaps temporally with surface ruptures at 9.8-10.5 ka on the central section (Leigh Lake earthquake LL2; Zellman, DuRoss, Thackray, et al., 2019) and 9.4-10.4 ka on the southern section (Buffalo Bowl earthquake BB3; DuRoss et al., 2019). Similar to BB3, SM2 likely predates the ~8 ka fan sediments exposed at Granite Canyon; DuRoss et al., 2019). Earthquake SM1 (5.2–5.9 ka) overlaps temporally with the most recent earthquakes previously interpreted on all three fault sections. SM1 is similar to earthquake BB1 at 3.9-5.7 ka on the southern section and overlaps with younger end of earthquake PDFs for earthquakes GC1 (4.8-7.8 ka) and LL1 (4.8-7.1). SM1 also has a similar time range to inferred event Snake River delta 2 (SRD2), on the northern section at 3.7-5.5 ka (Pierce et al., 1998; DuRoss et al., 2019). The Steamboat Mountain record suggests that the northern part of the Teton fault did not rupture in a younger post-4 ka earthquake, as weakly and indirectly suggested by SRD1 at 1.7-3.6 ka.

The timing of the youngest Teton fault surface rupture (herein, earthquake T1) is constrained by earthquake PDFs for the Buffalo Bowl (BB1), Granite Canyon (GC1), Leigh Lake (LL1), Snake River delta (SRD2), and Steamboat Mountain (SM1) sites (Fig. 10a,b). Temporal differences in these PDF data reflect geologic factors such as the geomorphic expression of faulting and types of depositional units exposed at the sites, as well as geochronological factors such as the type and number of ages used to constrain earthquake timing. BB1 and SRD2 yield 95% earthquake time ranges that overlap at 3.9-5.5 ka; however, the Buffalo Bowl results are based on a well-dated sequence of scarp colluvium and silt (DuRoss et al., 2019), whereas the timing of the Snake River delta disturbance event relies largely on the relative dating of cultural artifacts (Pierce et al., 1998). Both LL1 and GC1 yield broadly constrained PDFs, with 95% ranges that overlap at 4.8-7.1 ka. The broad timing constraints relate to coarse clastic material at these sites and limited maximum constraints on the most recent earthquake timing (Byrd, 1995; Zellman, DuRoss, Thackray, et al., 2019). As discussed earlier, the Steamboat Mountain site yields a high-fidelity record owing to abundant charcoal and fine-grained hanging-wall deposition and yields a highly dependable SM1 earthquake time of 5.2-5.9 ka.

To evaluate the timing of Teton fault earthquake T1, we combine the site earthquake data, following two approaches. First, we sum the probabilities for these PDFs (after Biasi and Weldon, 2009; DuRoss et al., 2011). This yields a broadly constrained summed earthquake PDF (shaded PDF; Fig. 10c) that spans the total uncertainty range of the constituent PDFs and has a mean of 5.4 ka and 95% confidence range of 3.9-7.4 ka. The summed PDF has a multimodal shape, but the peak probability is at 5.3 ka. The advantage of this model is that it captures the full range of the timing data; the disadvantage is that lower fidelity sites (e.g., GC1) are weighted equally with high fidelity sites (e.g., SM1). An alternative approach is to take the product of the probabilities in the overlapping parts of the site PDFs (solid line, Fig. 10b; after DuRoss et al., 2011). This method yields a product PDF with a mean of 5.3 ka and 95% range of 5.1-5.8 ka. The product PDF is unimodal with peak probability at 5.2 ka that decreases more gradually toward 5.8 ka than toward 5.1 ka. The advantage of this model is that it emphasizes the overlap in the constituent PDFs and is largely controlled by the highest-fidelity sites. The disadvantage is that it assumes that all site records offer accurate, independent observations of earthquake timing, which may not be the case.

Comparison with lacustrine paleoseismic data. The Teton fault lacustrine paleoseismic record from Jenny Lake (Fig. 1) yields a high-resolution event chronology, including nine turbidite disturbance horizons between ~14.0 and  $\sim$ 5.3 ka, with  $2\sigma$  uncertainties of 0.1–0.4 ka (Larsen et al., 2019), but is subject to several limitations. First, these data are limited to a single basin (Jenny Lake) and could include nontectonic events. Nontectonic turbidite triggering mechanisms, such as landslides formed during precipitation events or following variations in lake level related to outlet conditions or climate, are typically assessed using a multibasin approach (Monecke et al., 2004; Strasser et al., 2006, 2013; Howarth et al., 2014; Moernaut et al., 2014). Although Larsen et al. (2019) observed disturbance horizons that precede deposition of Mazama tephra (~7.6 ka) in multiple basins along the Teton fault (i.e., Leigh Lake, Phelps Lake, and Bradley Lake; Fig. 1), work to develop a multiple-basin event-correlation model is ongoing (D. Larsen, written comm., 2019).

An additional complexity lies in correlating Jenny Lake turbidite ages with the timing of surface rupture interpreted from terrestrial paleoseismic records. Although Jenny Lake turbidites yield narrow bounds on the timing of strong shaking in the basin, they cannot be explicitly linked to surface-faulting events on the Teton fault. Some disturbance horizons could also result from shaking related to other seismic sources in the region, such as the Grand Valley fault, Snake River caldera faults, or other faults associated with the Yellowstone caldera system. These sources are capable of generating shaking intensities of modified Mercalli intensity (MMI) > V, which can cause turbidity flows (Moernaut *et al.*, 2014). However, most turbidites form in

response to stronger shaking (MMI  $\geq$  VII; Monecke et al., 2004; Moernaut et al., 2014); thus, earthquakes on the Teton fault remain a likely trigger. Jenny Lake turbidites could form during earthquakes near the  $M_{\rm w} \sim 6.5$  threshold for surface faulting, which would generate strong shaking (e.g., MMI ≥ VII) near their epicenters. For example, although the 31 March 2020  $M_{\rm w}$  6.5 earthquake near Stanley, Idaho, likely did not generate surface rupture, the earthquake caused surface deformation, including an inlet delta failure in Stanley Lake (Z. Lifton, written comm., 2020; Data and Resources), consistent with modeled shaking intensities of MMI ≥ VII½ near the epicenter (Data and Resources). Along the Teton fault, a 15-18 km long surface rupture would likely generate an earthquake of  $M_{\rm w} \sim 6.5$  (Wells and Coppersmith, 1994; Wesnousky, 2008) and yield an ~17 km wide by ~35 km long, fault-parallel zone of strong shaking (MMI ≥ VII) that would be sufficient to cause turbidite formation in six basins from Phelps Lake to Moran Bay in Jackson Lake (Fig. S1, available in the supplemental material to this article). Such a rupture could occur along a portion of the Teton fault lacking terrestrial data, or generate only moderate (e.g., ≤0.5 m) displacement, below the resolution of detection in a traditional paleoseismic trench exposure given the coarse (e.g., glacial) sediment and the complex range front geomorphology.

Despite these limitations, we compare results from Steamboat Mountain with the Jenny Lake lacustrine record. The 9.7 ka mean age for SM2 corresponds well with a Jenny Lake turbidite at  $10.3 \pm 0.2$  ka  $(\pm 2\sigma)$ . The 10.3 ka Jenny Lake turbidite is well expressed in terms of sediment density and sand concentration (Larsen et al., 2019), an important consideration in that the Steamboat Mountain and Jenny Lake sites are ~29 km apart; thus, an event recorded at both sites would likely create stronger ground shaking and disrupt more sediment than a rupture localized at or near the site (e.g., restricted to the central section). However, using the 95% confidence range of 8.5-11.5 ka, SM2 also overlaps with disturbance horizons at 9.1  $\pm$  0.1 ka ( $\pm$ 2 $\sigma$ ) and 11.6  $\pm$  0.2 ka ( $\pm$ 2 $\sigma$ ) (Larsen et al., 2019). The 9.1 ka turbidite horizon has a similar sedimentological expression as the 10.3 ka event, and both are better expressed than the 11.6 ka horizon. Earthquake SM1 (5.2-5.9 ka; 95%) corresponds well with the youngest disturbance horizon exposed in the Jenny Lake core at  $5.3 \pm 0.2$  ka. These events have nearly identical time ranges: SM1 occurred at 5.2-5.9 ka (95%) and a Jenny Lake turbidite at 5.1-5.5 ka  $(2\sigma)$  (Fig. 10b). However, the youngest Jenny Lake turbidite is one of two that are weakly expressed in the Jenny Lake sedimentary record. Larsen et al. (2019) interpreted this weak signature as possibly reflecting a shorter and smaller-magnitude rupture of the Teton fault. However, considering the temporal overlap between SM1 and the Jenny Lake turbidite at ~5.3 ka, we consider it more likely that both event records correspond to a single Teton fault rupture.

We adopt a hybrid approach in which the youngest surfacerupturing earthquakes observed in terrestrial trench exposures are integrated with the high-resolution lacustrine chronology. The youngest Teton fault rupture (T1), which occurred at  $\sim$ 5.2–5.4 ka based on the mean and modal timing results from our summed and product PDFs, corresponds well with the youngest Jenny Lake disturbance horizon at  $5.3 \pm 0.2$  ka  $(2\sigma)$ (Larsen et al., 2019) (Fig. 10c). As a result, we adopt the simple explanation that Teton fault earthquake T1 occurred at ~5.3 ka, ruptured all five terrestrial sites, and generated a weakly expressed turbidite in Jenny Lake. An important caveat is that, considering the broadly defined terrestrial earthquake-timing uncertainties, we cannot distinguish between a single, long rupture of the Teton fault and separate, partial ruptures of the fault that overlap temporally. However, there is no obvious bias in the spatial distribution of young (<5 ka) versus older (>5 ka) timing data. Earthquake PDFs in support of a young (<5 ka) rupture (BB1 and SRD2) are from the southern and northern sections; earthquake PDFs supporting an older (>5 ka) rupture (GC1 and LL1) are from the southern and central sections (Fig. 10b). Finally, the highest fidelity sites (Jenny Lake and Steamboat Mountain) supporting the  $\sim$ 5.3 ka rupture are from the central and northern sections and ~29 km apart (Fig. 10b). Evaluating the sedimentary characteristics, thickness, and spatial extent of turbidites over multiple basins (Howarth et al., 2014; Moernaut et al., 2014) and through statistical means (e.g., Praet et al., 2020), in concert with analyses of terrestrial earthquake records, would help further refine earthquake rupture scenarios and shaking intensities.

Spatial constraints on rupture length and displacement. To evaluate the rupture length of the youngest Teton fault rupture (earthquake T1 at ~5.3 ka), we first define the southern and northern termini of the fault. The southern extent (Fig. 1) is well constrained based on new lidar-based mapping (Zellman, DuRoss, and Thackray, 2019). The northern terminus, north of Steamboat Mountain (Fig. 2), is defined by east-facing fault scarps that continue as far as 5.2 km north-northeast of the northernmost arm of Jackson Lake (4.6 km north-northeast of the Steamboat Mountain site; Fig. 2a; Zellman, DuRoss, and Thackray, 2019). These scarps are continuous, with the exception of two ~0.3-0.6 km wide gaps in the surface trace (Fig. 2b), and along their northernmost 2 km of length, form a horsetail bend to the northeast. Additional scarps and lineaments (black arrows; Fig. 2b) north of Steamboat Mountain could also be related to the Teton fault. However, these scarps face west and have arcuate geometries and are thus more likely associated with landslides moving northwest toward the Snake River Plain. East-facing scarps (black arrows; Fig. 2a) about 4-5 km north-northwest of the northern Teton fault terminus likely form the southernmost part of the Polecat Creek faults (part of the Snake River caldera faults; Ostenaa et al., 1993; Machette et al., 2001; Zellman, DuRoss, and Thackray, 2019) but could also have a gravitational origin.

Using these data, as well as the consistent decrease in bedrock range height from the central section of the Teton fault to the north (Smith et al., 1993), we interpret a total (maximum) Teton fault length of ~70 km (using the simplified trace of DuRoss et al., 2019), consistent with the mapping of Zellman, DuRoss, and Thackray (2019). This fault length corresponds with the extent of the uplifted footwall block of the Teton fault, which is defined from the center of the fault to the north by a decrease in elevation and Precambrian crystalline bedrock that is unconformably buried by Paleozoic sedimentary bedrock (Love et al., 1992; Smith et al., 1993; Byrd et al., 1994). A structural-geomorphic reconstruction by Brown et al. (2017) highlights the northsloping geometry of the unconformity. The region to the north of the Teton fault is heavily influenced by magmatic processes associated with the Yellowstone caldera: minimum principal stress directions rotate from east-west to northeast-southwest, between the northern Teton fault and the caldera boundary (White et al., 2009), and, the seismogenic thickness of the crust thins to less than ~5 km as a result of high heat flow (Smith and Braile, 1994; White et al., 2009; Huang et al., 2015).

Our synthesis of terrestrial and lacustrine paleoseismic data provides constraints on the rupture length and displacement of earthquake T1. We infer a total rupture length for earthquake T1 of ≥51 km and possibly ~70 km. The ≥51 km length is based on the distance between the Buffalo Bowl and Steamboat Mountain sites, whereas the ~70 km length is based on the mapped extent of the fault (Fig. 10d). Per-event vertical displacement along the Teton fault suggests consistently large, ~2 m surface displacements. For example, vertical displacement in Steamboat Mountain earthquakes SM2  $(2.0 \pm 1.0 \text{ m})$  and SM1  $(2.0 \pm 0.6 \text{ m})$  are similar to those recorded at the Buffalo Bowl, Granite Canyon, and Leigh Lake sites (mean of 2.1  $\pm$  0.5 m–1 $\sigma$ , Byrd, 1995; DuRoss *et al.*, 2019; Zellman, DuRoss, Thackray, et al., 2019). We combine these displacement data to infer mean displacement in earthquake T1 (Fig. 10d). Vertical displacement in earthquake T1 is, from south to north,  $2.1 \pm 0.4$  m (BB1),  $\sim 1.3$  m (GC1),  $1.4 \pm 0.3 \text{ m}$  (LL1), and  $2.0 \pm 0.6 \text{ m}$  (SM1) (Fig. 10d). We estimate that vertical displacement along the southern end of the fault is  $\sim 1.5 \pm 0.5$  m based on geomorphic mapping, which clearly shows postglacial fault scarps that are 3-5 m high and evidence for at least two earthquakes in trenches near Ski Lake (Zellman et al., 2020). Using these displacement data, the mean displacement for T1 is 1.7  $\pm$  1.0 m (errors propagated in quadrature, including an arbitrarily assigned 20% error for GC1). This estimate is subject to the limitations of the individual measurements and does not account for any lateral variability in displacement between the sites or a lateral decrease in displacement approaching the rupture termini.

### Implications of full-length Teton fault rupture

The complete,  $\sim$ 51–70 km long rupture of the Teton fault at  $\sim$ 5.3 ka has important implications for fault segmentation

and the frequency of rupture. Our data suggest that structural complexities along the fault did not impede the lateral propagation of rupture in the most recent Teton fault earthquake. These complexities consist of a branch fault along the southernmost 9 km of the fault (within the southern section), a 0.5-1.5 km wide left step between the southern and central sections, and a 2.5 km wide fault step with orthogonal cross faults between the central and northern sections. Historical surface-faulting earthquakes demonstrate that these types of features, as well as their spatial scales, can be found within the limits of dip-slip surface ruptures (Biasi and Wesnousky, 2016, 2017). For example, the 1915  $M_{\rm w}$  7.2 Pleasant Valley, Nevada, and 1887  $M_{\rm w}$  7.5 Sonora, Mexico, earthquake ruptures both include complex steps and bends along their traces (Wesnousky, 2008; Suter, 2015). These ruptures range in length from 61 km (Pleasant Valley) to >100 km (Sonora)—the longest recorded historic normalfault rupture (Suter, 2015). An additional full-length rupture of the Teton fault may have occurred at ~10 ka. This rupture is supported by terrestrial records from the southern (BB3;  $\sim$ 9.9 ka), central (LL2;  $\sim$ 10.0 ka), and northern (SM2;  $\sim$ 9.7 ka) sections, as well as a strong sedimentological signal in the Jenny Lake lacustrine data dated to ~10.3 ka.

We calculate moment magnitude estimates ( $M_{\rm w}$ ) for the 5.3 ka earthquake of 7.0–7.2. These estimates assume 51–70 km of rupture, with 1.7 m of mean vertical displacement, and range from  $M_{\rm w}$  7.0–7.1 based on seismic moment (Hanks and Kanamori, 1979; assuming a fault dip of 65°, seismogenic depth of 15 km, and rigidity of  $3 \times 10^{10}$  Pa) and  $M_{\rm w}$  7.0–7.2 based on all-fault-type magnitude regressions on surface rupture length (Wells and Coppersmith, 1994; Wesnousky, 2008). These results are similar to  $M_{\rm w}$  7.2 Teton fault earthquakes modeled by White *et al.* (2009) and Petersen *et al.* (2014).

Although available timing and displacement information suggest that earthquakes at ~10 and ~5.3 ka are most simply explained by full ruptures of the Teton fault, we cannot rule out partial fault ruptures. Partial ruptures are possible considering (1) the broad terrestrial earthquake-timing uncertainties, (2) the record of disturbance horizons at Jenny Lake, and (3) the global distribution of normal-faulting earthquake rupture lengths. First, individual earthquake-timing uncertainties for terrestrial earthquakes (e.g., SM1) are generally broad (>0.5 ka at 95% confidence) and allow for separate (partial) but temporally overlapping ruptures. Second, inconsistent terrestrial and lacustrine (Jenny Lake) paleoseismic data at  $\sim$ 8–9 ka highlight the potential for partial ruptures of the fault. Although an ~8 ka earthquake on the southern section (DuRoss et al., 2019) is supported by the Jenny Lake lacustrine data (~8.3 ka; Larsen et al., 2019), two additional earthquakes in the lacustrine record at ~9.1 and ~7.7 ka (Larsen et al., 2019) are not observed in the terrestrial paleoseismic record and could indicate partial ruptures of the central and/or northern fault sections. Alternatively, the ~9.1 and 7.7 ka lacustrine events could have been generated by Teton fault earthquakes below the magnitude threshold for surface faulting ( $M_{\rm w}\sim 6.5$  or less; dePolo, 1994; Wells and Coppersmith, 1994). Finally, although the ~70 km length of the Teton fault is consistent with several historical ruptures (e.g., Wesnousky, 2008), this length exceeds the mean length of historical normal-faulting earthquakes globally ( $30\pm 17~{\rm km}-1\sigma$ , based on data in Wells and Coppersmith, 1994; Wesnousky, 2008). Thus, similar to that for other long normal faults, such Wasatch fault zone (DuRoss *et al.*, 2016), partial ruptures should not be discounted.

Partial ruptures of the Teton fault help clarify differences in earthquake recurrence derived from terrestrial and lacustrine earthquake records. Jenny Lake lacustrine data have been interpreted as recording major fault ruptures with a postglacial mean recurrence of  $1.1 \pm 0.3$  ky  $(1\sigma)$  (Larsen et al., 2019), compared with a terrestrial-record mean of 2.4 ky, based on three surfacerupturing earthquakes between ~10.0 and ~5.3 ka (similar to DuRoss et al., 2019). Given this apparent disagreement in recurrence, we hypothesize that the lacustrine record, which integrates shaking from all sources at a point, includes partial failures that is, smaller magnitude ruptures—of the central Teton fault, some of which may not be included in the terrestrial record. For example, an ~18 km long rupture of the fault with  $M_{\rm w}$  ~ 6.5 would generate sufficient shaking (MMI ≥ VII) to generate turbidites along the entire central section (Fig. S1). In the 2018 U.S. Geological Survey (USGS) National Seismic Hazard Model (NSHM; Petersen et al., 2019), the on-fault recurrence of  $M_w$  6.5 earthquakes summed over all branches of the logic tree for the Teton fault is  $\sim 0.8$  ky (P. Powers, written comm., 2020). The  $\sim$ 0.8 ka recurrence of  $M_{\rm w}$  6.5 earthquakes, which are small enough that they may not generate surface rupture but large enough to cause shaking intensities that result in turbidites, is sufficient to explain the variation in the surface-faulting (terrestrial) and shaking (lacustrine) records.

To reconcile the long, infrequent ruptures suggested by the terrestrial data with more frequent and possibly shorter ruptures supported by the lacustrine data, we advocate for a model of bimodal rupture behavior. That is, we propose a model of both partial and complete ruptures of the fault yielding earthquakes of  $M_{\rm w} \sim 6.5$ –7.2 at minimum every  $\sim 1.2$  ky. The largest magnitude ruptures, of which two are clearly recorded across ≥51 km of the Teton fault (DuRoss et al., 2019; this study), would likely be recorded by sediment disturbance in all regional lakes. In contrast, smaller ruptures would be recorded most easily in lakes nearest the event. Both terrestrial and lacustrine datasets have potential weaknesses: several factors could contribute to incomplete terrestrial paleoseismic records (e.g., coarse sediment, complex exposures, and age scatter), and lacustrine sediment may record more than just surface-faulting earthquakes (e.g., precipitation-induced landsliding or strong shaking from non-surfacerupturing earthquakes or earthquakes on other regional faults). Assuming these issues have been considered carefully, the terrestrial and lacustrine data at face value still yield significantly different recurrence estimates. However, complete rupture of the fault at ~10 and 5.3 ka, with three additional partial ruptures of the fault between ~8 and 9 ka, would yield a mean recurrence of ~1.2 ky (five earthquakes between ~10 and 5.3 ka), possibly reconciling the two datasets. Considering these different modes of rupture, we propose that the boundaries between the southern, central, and northern fault sections are ephemeral (after Philibosian and Meltzner, 2020)—serving as lateral rupture boundaries in response to the state of stress along the fault (possibly changing between seismic cycles) rather than long-lasting structural controls.

The bimodal earthquake behavior of the Teton fault is broadly consistent with the characterization of the fault in the USGS NSHMs, which includes both full-source ( $M_{\rm w}$  7.2) and partial-source ( $M_{\rm w}$  6.5–7.2) ruptures. As the latter are modeled using Gutenberg–Richter recurrence, the integrated recurrence of partial-to-complete  $M_{\rm w}$  6.5–7.2 ruptures, derived from lacustrine and terrestrial data, would serve as an incremental improvement to the NSHM. Additional terrestrial and lacustrine data for the Teton fault, targeted along the central and northern sections of the fault, could serve to refine estimates of fault rupture extent and earthquake recurrence and test the bimodal rupture hypothesis.

### CONCLUSIONS

We use paleoseismic data obtained from two trenches at the Steamboat Mountain site to constrain the timing, displacement, length, and magnitude of Holocene ruptures of the Teton fault. Two postglacial surface-faulting earthquakes at the site have resulted in distinct periods of down-to-the-east surface-faulting, scarp-derived colluvial sedimentation, and hanging-wall burial by fine-grained alluvial-fan deposits. Bayesian modeling of a stratigraphically consistent sequence of radiocarbon ages yields earthquake times of ~5.5 ka (SM1) and ~9.7 ka (SM2) and an earthquake record at the site that is complete since ~9-11 ka. Earthquakes SM1 and SM2—each generated ~2 m of vertical displacement at Steamboat Mountain based on the site geomorphology and exposure of hanging-wall sedimentary units. We compare these results with previous terrestrial and lacustrine paleoseismic data and conclude that the Teton fault ruptured in its entirety ( $\sim$ 51-70 km) in an  $M_{\rm w}$  7.0-7.2 earthquake, at ~5.3 ka. This youngest Teton fault earthquake likely generated surface rupture at five paleoseismic sites and along three sections of the fault; thus, we conclude that structural complexities along the fault (i.e., a branch fault, fault step, and bend) did not impede its lateral propagation. A similar, complete rupture of the Teton fault is possible at ~10 ka; however, partial ruptures of the fault at ~8-9 ka and limited laterally by ephemeral rupture boundaries help reconcile the terrestrial and lacustrine paleoseismic data. We propose a bimodal rupture hypothesis of alternating full-length and incomplete ruptures of the fault, yielding  $M_{\rm w} \sim$ 6.5-7.2 earthquakes every ~1.2 ky, which could help refine regional seismic hazard models and be tested using additional terrestrial and lacustrine paleoseismic data.

### **DATA AND RESOURCES**

Figure 1 includes a 30-m-resolution digital elevation model basemap available at https://viewer.nationalmap.gov/basic/. In Figures 2-4, basemaps are derived from 1 m resolution light detection and ranging (lidar) data collected in 2014 by Grand Teton National Park (GRTE) and provided by the National Park Service (NPS) office in Moose, Wyoming. Information on observed and modeled shaking intensities and ground failures in the 2020  $M_{\rm w}$  6.5 Stanley, Idaho, earthquake is available https://earthquake.usgs.gov/earthquakes/eventpage/us70008jr5/ executive. Observations of secondary effects, such as landslides and avalanches related to the Stanley earthquake, are available at https:// www.idahogeology.org/stanley-earthquake and http://learningfrom earthquakes.org/2020-03-31\_challisidaho/. All websites were last accessed in June 2020. All other data and resources used in this study are listed and cited in the article. The Appendix includes descriptions of stratigraphic units exposed in Steamboat Mountain trenches A and B. The supplemental material includes OxCal Bayesian modeling code used to generate earthquake timing data for the Steamboat Mountain site as well as contours of modified Mercalli intensity generated in an  $M_{\rm w}$  6.5 Teton fault earthquake scenario.

### **ACKNOWLEDGMENTS**

This work was funded by the University of Wyoming—National Park Service Small Grants Research Program, the U.S. Geological Survey (USGS) Earthquake Hazards Program, Idaho State University, and BGC Engineering, Inc. Tyler Reyes, Nicole Cholewinski, and Nick Patton provided able field assistance and helped move tons of sediment. The authors thank Simeon Caskey, Kathy Melander, Katherine Birmingham, Elizabeth Barrett, and Breelyn Van Fleet of the U.S. National Park Service, for ongoing interest in their research and for their assistance with site permitting. The authors thank Jeanne Godaire, Ralph Klinger, Kris Hornsby, and Darren Larsen, for visiting the Steamboat Mountain paleoseismic study site and discussing the trench exposures. The authors also thank David Wald for producing the  $M_{\rm w}$  6.5 Teton fault earthquake scenario and derivative products. Dean Ostenaa and Rob Witter provided review comments on an early version of this article that helped strengthen the article. This article also benefited from constructive reviews provided by Stephen Angster, Rich Koehler, an anonymous BSSA reviewer, and Associate Editor Nicola Litchfield. Any use of trade, firm, or product names is for descriptive purposes only and does not imply endorsement by the U.S. Government.

### **REFERENCES**

- Biasi, G. P., and R. J. Weldon (2009). San Andreas fault rupture scenarios from multiple Paleoseismic records: Stringing pearls, *Bull. Seismol. Soc. Am.* 99, no. 2A, 471–498, doi: 10.1785/0120080287.
- Biasi, G. P., and S. G. Wesnousky (2016). Steps and gaps in ground ruptures: Empirical bounds on rupture propagation, *Bull. Seismol. Soc. Am.* **106**, no. 3, 1110–1124, doi: 10.1785/0120150175.
- Biasi, G. P., and S. G. Wesnousky (2017). Bends and ends of surface ruptures, *Bull. Seismol. Soc. Am.* **107**, no. 6, 2543–2560, doi: 10.1785/0120160292.
- Bronk Ramsey, C. (2009). Bayesian analysis of radiocarbon dates, *Radiocarbon* **51**, no. 1, 337–360, doi: 10.1017/S0033822200033865.
- Brown, S. J., J. R. Thigpen, J. A. Spotila, W. C. Krugh, L. M. Tranel, and D. A. Orme (2017). Onset timing and slip history of the Teton

- fault, Wyoming: A multidisciplinary reevaluation, *Tectonics* **36**, no. 11, 2669–2692, doi: 10.1002/2016TC004462.
- Byrd, J. O. D. (1995). Neotectonics of the Teton fault, Wyoming, *Doctoral Dissertation*, University of Utah, Salt Lake City, Utah.
- Byrd, J. O. D., R. B. Smith, and J. W. Geissman (1994). The Teton fault, Wyoming: Topographic signature, neotectonics, and mechanism of deformation, *J. Geophys. Res.* **99**, no. B10, 20,095–20,122.
- Christiansen, R. L. (1984). Yellowstone magmatic evolution: Its bearing on understanding large-volume explosive volcanism, in *Explosive Volcanism*, Its Inception, Evolution and Hazards, National Academy Press, National Research Council Studies in Geophysics, Washington D.C., 84–95.
- Christiansen, R. L. (2001). The Quaternary and Pliocene Yellowstone Plateau Volcanic Field of Wyoming, Idaho, and Montana, *U.S. Geol. Surv. Prof. Pap. 729-G*, G1–G145.
- DePolo, C. M. (1994). The maximum background earthquake for the basin and range province, western North America, *Bull. Seismol. Soc. Am.* **84**, no. 2, 466–472.
- DuRoss, C. B., S. E. K. Bennett, R. W. Briggs, S. F. Personius, R. D. Gold, N. G. Reitman, A. I. Hiscock, and S. A. Mahan (2018). Combining conflicting Bayesian models to develop paleoseismic records: An example from the Wasatch fault zone, Utah, *Bull. Seismol. Soc. Am.* 108, no. 6, 3180–3201, doi: 10.1785/0120170302.
- DuRoss, C. B., R. D. Gold, R. W. Briggs, J. E. Delano, D. A. Ostenaa, M. S. Zellman, N. Cholewinski, S. J. Wittke, and S. A. Mahan (2019). Holocene earthquake history and slip rate of the southern Teton fault, Wyoming, USA, Geol. Soc. Am. Bull. 132, nos. 7/8, 1566–1586, doi: 10.1130/B35363.1.
- DuRoss, C. B., S. F. Personius, A. J. Crone, S. S. Olig, M. D. Hylland, W. R. Lund, and D. P. Schwartz (2016). Fault segmentation: New concepts from the Wasatch Fault Zone, Utah, USA: Central Wasatch Fault Zone Segmentation, J. Geophys. Res. 121, no. 2, 1131–1157, doi: 10.1002/2015JB012519.
- DuRoss, C. B., S. F. Personius, A. J. Crone, S. S. Olig, and W. R. Lund (2011). Integration of paleoseismic data from multiple sites to develop an objective earthquake chronology: Application to the weber segment of the Wasatch fault Zone, Utah, *Bull. Seismol. Soc. Am.* 101, no. 6, 2765–2781, doi: 10.1785/0120110102.
- Field, E. H., R. J. Arrowsmith, G. P. Biasi, P. Bird, T. E. Dawson, K. R. Felzer, D. D. Jackson, K. M. Johnson, T. H. Jordan, C. Madden, et al. (2014). Uniform California Earthquake Rupture Forecast, Version 3 (UCERF3)—The time-independent model, Bull. Seismol. Soc. Am. 104, no. 3, 1122–1180, doi: 10.1785/0120130164.
- Galbraith, R. F. (2010). On plotting OSL equivalent doses, *Ancient TL* **28**, no. 1, 1–10.
- Gilbert, J. D., D. A. Ostenaa, and C. Wood (1983). Seismotectonic study Jackson Lake Dam and Reservoir, Minidoka Project, Idaho-Wyoming: Denver, Colorado, U.S. Department of the Interior, U.S. Bureau of Reclamat. Seismotectonic Rept. 83-8, 123 pp.
- Gray, H. J., S. A. Mahan, T. Rittenour, and M. S. Nelson (2015). Guide to luminescence dating techniques and their application for paleoseismic research, *Proc. Volume, Basin and Range Province Seismic Hazards Summit III (BRPSHSIII)*, Utah Geol. Surv. Misc. Pub. 15– 5, Salt Lake City, Utah, 12–17 January 2015, variously paginated.
- Hanks, T. C., and H. Kanamori (1979). A moment magnitude scale, *J. Geophys. Res.* **84**, no. B5, 2348–2350.

- Houston, D. B. (1973). Wildfires in northern Yellowstone National Park, Ecology 54, no. 5, 1111–1117.
- Howarth, J. D., S. J. Fitzsimons, R. J. Norris, and G. E. Jacobsen (2014). Lake sediments record high intensity shaking that provides insight into the location and rupture length of large earthquakes on the Alpine Fault, New Zealand, *Earth Planet. Sci. Lett.* 403, 340–351, doi: 10.1016/j.epsl.2014.07.008.
- Huang, H.-H., F.-C. Lin, B. Schmandt, J. Farrell, R. B. Smith, and V. C. Tsai (2015). The Yellowstone magmatic system from the mantle plume to the upper crust, *Science* **348**, no. 6263, 773–776.
- Lageson, D. R. (1992). Possible Laramide influence on the Teton normal fault, western Wyoming, in *Geological Society of America Memoirs*, Geological Society of America, 183–196.
- Larsen, D. J., S. E. Crump, M. B. Abbott, W. Harbert, A. Blumm, N. J. Wattrus, and J. J. Hebberger (2019). Paleoseismic evidence for climatic and magmatic controls on Teton Fault, *Geophys. Res. Lett.* 46, 13,036–13,043, doi: 10.1029/2019GL085475.
- Larsen, D. J., M. S. Finkenbinder, M. B. Abbott, and A. R. Ofstun (2016). Deglaciation and postglacial environmental changes in the Teton Mountain Range recorded at Jenny Lake, Grand Teton National Park, WY, Quaternary Sci. Rev. 138, 62–75, doi: 10.1016/j.quascirev.2016.02.024.
- Licciardi, J. M., and K. L. Pierce (2018). History and dynamics of the Greater Yellowstone Glacial System during the last two glaciations, *Quaternary Sci. Rev.* 200, 1–33, doi: 10.1016/j.quascirev.2018.08.027.
- Loope, L. L., and G. E. Gruell (1973). The ecological role of fire in the Jackson Hole area, northwestern Wyoming, *Quaternary Res.* **3**, 425–443.
- Love, J. D., J. C. Reed, and A. C. Christiansen (1992). Geologic Map of Grand Teton National Park, Teton County, Wyoming, U.S. Geological Survey Misc. Invest. Series, U. S. Geological Survey, 1:62,500.
- Machette, M. N., K. L. Pierce, J. P. McCalpin, K. M. Haller, and R. L. Dart (2001). Map and data for Quaternary faults and folds in Wyoming, U.S. Geol. Surv. Open-File Rept. 01-461, 154 pp, scale 1:750000.
- Millspaugh, S. H., and C. Whitlock (1995). A 750-year fire history based on lake sediment records in central Yellowstone National Park, USA, *Holocene* 5, no. 3, 283–292.
- Moernaut, J., M. Van Daele, K. Heirman, K. Fontijn, M. Strasser, M. Pino, R. Urrutia, and M. De Batist (2014). Lacustrine turbidites as a tool for quantitative earthquake reconstruction: New evidence for a variable rupture mode in south central Chile, *J. Geophys. Res.* 119, 1607–1633, doi: 10.1002/2013JB010738.
- Monecke, K., F. S. Anselmetti, A. Becker, M. Sturm, and D. Giardini (2004). The record of historic earthquakes in lake sediments of Central Switzerland, *Tectonophysics* 394, 21–40, doi: 10.1016/ j.tecto.2004.07.053.
- Nelson, A. R. (1992). Lithofacies analysis of colluvial sediments—An aid in interpreting the recent history of Quaternary normal faults in the Basin and Range Province, Western United States, *J. Sed. Pet.* **62**, no. 4, 607–621, doi: 10.1306/D426796F-2B26-11D7-8648000102C1865D.
- O'Connell, D. R. H., C. K. Wood, D. A. Ostenaa, L. V. Block, and R. C. LaForge (2003). Ground motion evaluation for Jackson Lake Dam, Minidoka project, Wyoming: Denver, Colorado, *Bureau Reclamat. Rept.* 2003-2, 493 pp.
- Ostenaa, D. A., C. Wood, and J. D. Gilbert (1993). Seismotectonic Study for Grassy Lake Dam – Minidoka Project, Wyoming, Bureau Reclamat. Seismotectonic Rept. 93-3, 68 pp.

- Petersen, M. D., M. P. Moschetti, P. M. Powers, C. S. Mueller, K. M. Haller, A. D. Frankel, Y. Zeng, S. Rezaeian, S. C. Harmsen, O. S. Boyd, et al. (2014). Documentation for the 2014 update of the United States national seismic hazard maps, U.S. Geol. Surv. Open-File Rept. 2014-1091, 243 pp., doi: 10.3133/ofr20141091.
- Petersen, M. D., A. M. Shumway, P. M. Powers, C. S. Mueller, M. P. Moschetti, A. D. Frankel, S. Rezaeian, D. E. McNamara, N. L. Luco, O. S. Boyd, *et al.* (2019). The 2018 update of the US National seismic hazard model: Overview of model and implications, *Earthq. Spectra* 36, no. 1, 5–41.
- Philibosian, B., and A. J. Meltzner (2020). Segmentation and supercycles: A catalog of earthquake rupture patterns from the Sumatran Sunda Megathrust and other well-studied faults worldwide, *Quaternary Sci. Rev.* **241**, 1–43, doi: 10.1016/j.quascirev.2020.106390.
- Pierce, K. L., J. M. Licciardi, J. M. Good, and C. Jaworowski (2018). Pleistocene glaciation of the Jackson Hole area, Wyoming, U.S. Geol. Surv. Prof. Pap. 1835, 56 pp., doi: 10.3133/pp1835.
- Pierce, K. L., S. Lundstrom, and J. M. Good (1998). Geological setting of archeological sites in the Jackson Lake area, Wyoming, in M. A. Conner (Editor), Final Rept. the Jackson Lake Archeol. Project, U.S. Bureau of Reclamat. Tech. Rept. 46, Grant Teton National Park, Wyoming, Boise, Idaho, 29–48.
- Praet, N., M. Van Daele, T. Collart, J. Moernaut, E. Vandekerkhove, P. Kempf, P. J. Haeussler, and M. De Batist (2020). Turbidite stratigraphy in proglacial lakes: Deciphering trigger mechanisms using a statistical approach, Sedimentology 67, doi: 10.1111/sed.12703.
- Reitman, N. G., S. E. K. Bennett, R. D. Gold, R. W. Briggs, and C. B. DuRoss (2015). High-resolution trench photomosaics from image-based modeling: Workflow and error analysis, *Bull. Seismol. Soc. Am.* 105, no. 5, 2354–2366, doi: 10.1785/0120150041.
- Rhodes, E. J. (2011). Optically stimulated luminescence dating of sediments over the past 200,000 years, *Annu. Rev. Earth Planet. Sci.* **39**, no. 1, 461–488, doi: 10.1146/annurev-earth-040610-133425.
- Scharer, K., R. Weldon, A. Streig, and T. Fumal (2014). Paleoearthquakes at Frazier Mountain, California delimit extent and frequency of past San Andreas Fault ruptures along 1857 trace: New rupture history of San Andreas Fault, *Geophys. Res. Lett.* 41, no. 13, 4527–4534, doi: 10.1002/2014GL060318.
- Scharer, K. M., and D. Yule (2020). A maximum rupture model for the southern San Andreas and San Jacinto faults, California, derived from paleoseismic earthquake ages: Observations and limitations, *Geophys. Res. Lett.* 47, 1–11, doi: 10.1029/2020GL088532.
- Schwartz, D. P., and K. J. Coppersmith (1984). Fault behavior and characteristic earthquakes: Examples from the Wasatch and San Andreas fault zones, *J. Geophys. Res.* **89**, no. B7, 5681–5698, doi: 10.1029/JB089iB07p05681.
- Smith, R. B., and L. W. Braile (1994). The Yellowstone hotspot, J. Volcan. Geoth. Res. 61, 121–187.
- Smith, R. B., J. O. D. Byrd, and D. D. Susong (1990). Neotectonics and structural evolution of the Teton fault, in S. Roberts (Editor), Geologic Field Tours of Western Wyoming, Geol. Surv. Wyoming Public Information Circular 29, 127–138.
- Smith, R. B., J. O. D. Byrd, and D. D. Susong (1993). The Teton fault, Wyoming: Seismotectonics, Quaternary history, and earthquake hazards, in Geology of Wyoming, Geol. Surv. Wyoming Memoir No. 5, 628–667.

- Smith, R. B., M. Jordan, B. Steinberger, C. M. Puskas, J. Farrell, G. P. Waite, S. Husen, W.-L. Chang, and R. O'Connell (2009). Geodynamics of the Yellowstone hotspot and mantle plume: Seismic and GPS imaging, kinematics, and mantle flow, *J. Volcan. Geoth. Res.* 188, 26–56, doi: 10.1016/j.jvolgeores.2009.08.020.
- Strasser, M., F. S. Anselmetti, D. Fäh, D. Giardini, and M. Schnellmann (2006). Magnitudes and source areas of large prehistoric northern Alpine earthquakes revealed by slope failures in lakes, *Geology* **34**, no. 12, 1005–1008, doi: 10.1130/G22784A.1.
- Strasser, M., K. Monecke, M. Schnellmann, and F. S. Anselmetti (2013). Lake sediments as natural seismographs: A compiled record of Late Quaternary earthquakes in Central Switzerland and its implication for Alpine deformation, *Sedimentology* 60, 319–341, doi: 10.1111/sed.12003.
- Suter, M. (2015). Rupture of the Pitáycachi Fault in the 1887 M w 7.5 Sonora, Mexico earthquake (southern Basin-and-Range Province): Rupture kinematics and epicenter inferred from rupture branching patterns, *J. Geophys. Res.* 120, no. 1, 617–641, doi: 10.1002/2014JB011244.
- Thackray, G. D., and A. E. Staley (2017). Systematic variation of Late Pleistocene fault scarp height in the Teton Range, Wyoming, USA: Variable fault slip rates or variable landform ages? *Geosphere* 13, no. 2, 287–300, doi: 10.1130/GES01320.1.
- Valentini, A., C. B. DuRoss, E. H. Field, R. D. Gold, R. W. Briggs, F. Visini, and B. Pace (2019). Relaxing segmentation on the Wasatch fault zone: Impact on seismic hazard, *Bull. Seismol. Soc. Am.* 110, no. 1, 83–109, doi: 10.1785/0120190088.
- Wells, D. L., and K. J. Coppersmith (1994). New empirical relationships among magnitude, rupture length, rupture width, rupture area, and surface displacement, *Bull. Seismol. Soc. Am.* 84, no. 4, 974–1002.

- Wesnousky, S. G. (2008). Displacement and geometrical characteristics of earthquake surface ruptures: Issues and implications for seismic-hazard analysis and the process of earthquake rupture, *Bull. Seismol. Soc. Am.* **98,** no. 4, 1609–1632, doi: 10.1785/0120070111.
- White, B. J. P., R. B. Smith, S. Husen, J. M. Farrell, and I. Wong (2009). Seismicity and earthquake hazard analysis of the Teton–Yellowstone region, Wyoming, *J. Volcan. Geoth. Res.* **188**, nos. 1/3, 277–296, doi: 10.1016/j.jvolgeores.2009.08.015.
- Working Group on Utah Earthquake Probabilities (Editor) (2016). Earthquake probabilities for the Wasatch Front region in Utah, Idaho, and Wyoming, *Utah*, *Utah Geol. Surv. Misc. Pub. 16-3*, Utah Geological Survey, Salt Lake City, Utah, 418 pp.
- Zellman, M. S., C. B. DuRoss, R. D. Gold, G. D. Thackray, S. J. Wittke, J. E. Delano, J. Mauch, I. Medina, R. Phillips, E. Collins, et al. (2020). Does the Phillips Valley fault rupture with the Teton fault? (abstract), Seismol. Res. Lett. 91, no. 2B, 1192.
- Zellman, M. S., C. B. DuRoss, and G. D. Thackray (2019). The Teton fault, Teton County, Wyoming, Open-File Rept. 2019-01, Wyoming Geol. Surv. Open-File Rept. 2019-01, Wyoming Geological Survey, scale 1:75,000.
- Zellman, M. S., C. B. DuRoss, G. D. Thackray, S. F. Personius, N. G. Reitman, S. A. Mahan, and C. C. Brossy (2019). Holocene rupture history of the Central Teton Fault at Leigh Lake, Grand Teton National Park, Wyoming, Bull. Seismol. Soc. Am. 110, no. 1, 67–82.

### **APPENDIX**

This Appendix includes Table A1 comprising descriptions of stratigraphic units at the Steamboat Mountain paleoseismic site, Teton fault, Wyoming.

### TABLE A1

### Descriptions of Stratigraphic Units within Trenches A and B, Steamboat Mountain Trench Site

### **Unit Description**

Trench A

- Soil A horizon. Massive and poorly sorted sandy loam at the surface in both the hanging wall and footwall of the fault. Sharp and wavy basal contact. Clasts are subangular to subrounded; 3 cm maximum; 0.5 cm average. Nonplastic; weak cementation. Dry color: 10YR 4/2. 35% fines, 55% sand (coarse), 10% gravel, 0% cobbles/boulders
- Alluvial-fan sediment. Moderately bedded and sorted gravely, silty sand in the fault hanging wall. Sharp basal contact. Clasts are subangular to subrounded; 5 cm maximum; 1 cm average. Nonplastic; good cementation. Dry color: 10YR 5/2. 10% fines, 75% sand (coarse), 15% gravel, 0% cobbles/boulders
- Alluvial-fan sediment with paleosol. Weakly bedded and moderately sorted gritty, sandy silt with fine interbeds in the fault hanging wall. Includes charcoal-rich A horizon within uppermost part of unit. Diffuse to sharp basal contact (locally with fine sand). Clasts are subangular; 1 cm maximum; 0.4 cm average. Slightly plastic; moderate-to-good cementation. Dry color: 10YR 5/2; moist color: 10YR 3/3. 60% fines, 35% sand (medium-coarse), 5% gravel, 0% cobbles/boulders
- Alluvial-fan sediment. Massive and poorly to moderately sorted gritty, sandy silt in the fault hanging wall. Diffuse basal contact. Clasts are subangular; 2 cm maximum; 0.5 cm average. Slightly plastic; moderate cementation. Moist color: 10YR 4/3. 55% fines, 40% sand (medium–coarse), 5% gravel, 0% cobbles/boulders
- Scarp-derived colluvium. Massive and poorly sorted gravely, sandy silt in the fault hanging wall. Diffuse to sharp (at eroded fault-scarp free face) basal contact. Clasts are subangular to well rounded; 20 cm maximum; 10 cm average. Slightly plastic; moderate cementation. Dry color: 10YR 5/2; moist color: 10YR 3/3. 55% fines, 30% sand (medium–coarse), 5% gravel, 10% cobbles/boulders
- Alluvial-fan sediment with paleosol. Massive and moderately sorted sandy silt with pebbles in the fault hanging wall. Includes charcoal-rich A horizon within uppermost part of unit. Sharp basal contact. Clasts are subangular; 3 cm maximum; 1 cm average. Slightly plastic; moderate cementation. Moist color: 10YR 2/2. 60% fines, 35% sand (medium–coarse), 5% gravel, 0% cobbles/boulders

(continued)

### **Unit Description**

- C2 Scarp-derived colluvium. Massive and poorly sorted gravely, sandy silt in the fault hanging wall. Sharp basal contact. Clasts are subangular; 20 cm maximum; 4 cm average. Slightly plastic; moderate cementation. Moist color: 10YR 3/3. 70% fines, 20% sand (medium–coarse), 5% gravel, 5% cobbles/boulders
- SS Sheared sediment. Massive and moderately sorted gravely silt with grit in the fault shear zone. Basal contact not exposed. Clasts are subangular; 0.2 cm maximum; 0.1 cm average. Plastic; moderate cementation. Moist color: 10YR 3/3. 80% fines, 20% sand (fine–coarse), 0% gravel, 0% cobbles/boulders
- Glaciofluvial sediment. Massive and very poorly sorted sandy gravel/diamict in the fault footwall. Diffuse basal contact. Clasts are subangular to well rounded; 120 cm maximum; 20 cm average. Nonplastic; moderate cementation. Dry color: 10YR 5/2; moist color: 10YR 4/2. 5% fines, 40% sand (coarse), 20% gravel, 35% cobbles/boulders
- Glaciofluvial sediment. Weakly bedded and moderately to poorly sorted silty sand in the fault footwall. Sharp, wavy basal contact. Clasts are subangular to subrounded; 1 cm maximum; 0.7 cm average. Nonplastic; no cementation. Dry color: 10YR 5/3; moist color: 10YR 4/3. 20% fines, 75% sand (fine–coarse), 5% gravel, 0% cobbles/boulders
- Glaciofluvial sediment. Upper of two subunits within unit 12. Weakly bedded and poorly sorted silty, sandy gravel in the fault footwall. Diffuse basal contact. Clasts are subangular to well rounded; 18 cm maximum; 4 cm average. Nonplastic; no cementation. Dry color: 10YR 5/2; moist color: 10YR 4/3. 10% fines, 65% sand (medium–coarse), 20% gravel, 5% cobbles/boulders
- Glaciofluvial sediment. Lower of two subunits within unit 12. Moderately bedded and moderately sorted sandy silt and silty sand in the fault footwall. Diffuse basal contact. Clasts are subrounded; 6 cm maximum; 3 cm average. Slightly plastic; weak cementation. Dry color: 10YR 6/2; moist color: 10YR 4/3. 45% fines, 50% sand (medium–coarse), 5% gravel, 0% cobbles/boulders
- Glaciofluvial sediment. Moderately bedded and moderately sorted sand and gravel in the fault footwall. Sharp basal contact. Clasts are subangular to well rounded; 10 cm maximum; 5 cm average. Nonplastic; no to weak cementation. Dry color: 10YR 6/2; moist color: 10YR 3/4. 5% fines, 45% sand (medium–coarse), 30% gravel, 20% cobbles/boulders
- Glaciofluvial sediment. Weakly bedded and moderately to well sorted sand and silt in the fault footwall. Basal contact not exposed. Clasts are subangular to subrounded; 10 cm maximum; 6 cm average. Moderately plastic; weak cementation. Moist color: 10YR 4/3. 45% fines, 45% sand, 5% gravel, 5% cobbles/boulders

#### Trench B

- Slope wash. Massive and poorly sorted sandy loam at the surface in the fault footwall. Diffuse basal contact. Clasts are subangular; 2 cm maximum; 1 cm average. Nonplastic; moderate cementation. Dry color: 10YR 4/3; moist color 10YR 3/2. 45% fines, 50% sand (coarse), 5% gravel, 0% cobbles/boulders
- Soil A horizon. Massive and moderately sorted sandy, clayey silt in the fault footwall. Sharp basal contact. Slightly plastic; no cementation. Dry color: 10YR 4/3; moist color: 10YR 2/2. 80% fines, 20% sand (medium), 0% gravel, 0% cobbles/boulders
- 41 Alluvial-fan sediment with paleosol. Very weakly bedded and well sorted clayey silt paleosol in the fault hanging wall. Diffuse basal contact. Plastic; weak to moderate cementation. Moist color: 10YR 3/2. 85% fines, 15% sand (fine), 0% gravel, 0% cobbles/boulders
- 40 Alluvial-fan sediment. Massive and well sorted medium silt in the fault hanging wall. Diffuse basal contact. Plastic; weak to moderate cementation. Moist color: 10YR 4/3. 85% fines, 15% sand (very fine–fine), 0% gravel, 0% cobbles/boulders
- Alluvial-fan sediment. Massive to very weakly bedded and poorly to moderately sorted silt with gravel in the fault hanging wall. Gradational basal contact. Clasts are subangular; 3 cm maximum; 0.5 cm average. Slightly plastic; moderate-to-strong cementation. Dry color: 10YR 5/2; moist color 10YR 4/2. 50% fines, 45% sand (medium–coarse), 5% gravel, 0% cobbles/boulders
- Alluvial-fan sediment. Upper of two subunits within unit 38. Moderately bedded and well sorted silty, very fine sand in the fault hanging wall. Sharp basal contact. Slightly plastic; moderate-to-strong cementation. Moist color: 10YR 5/3. 60% fines, 40% sand (very fine), 0% gravel, 0% cobbles/boulders
- Alluvial-fan sediment. Lower of two subunits within unit 38. Well bedded and moderately sorted silty sand in the fault hanging wall. Sharp basal contact. Clasts are subangular; 0.6 cm maximum; 0.4 cm average. Nonplastic; moderate-to-strong cementation. Moist color: 10YR 5/3. 10% fines, 85% sand (coarse–very coarse), 5% gravel, 0% cobbles/boulders
- Alluvial-fan sediment. Massive and moderately to well sorted clayey silt in the fault hanging wall. Sharp basal contact. Plastic; moderate cementation. Moist color: 10YR 3/2. 90% fines, 10% sand (very fine), 0% gravel, 0% cobbles/boulders
- Alluvial-fan sediment. Well bedded and moderately sorted sandy silt in the fault hanging wall. Sharp basal contact. Clasts: 0.2 cm maximum; 0.2 cm average. Slightly plastic; weak cementation. Moist color: 10YR 5/3. 60% fines, 35% sand (medium–coarse), 5% gravel, 0% cobbles/boulders
- Alluvial-fan sediment. Massive and moderately to well sorted clayey silt in the fault hanging wall. Diffuse to sharp basal contact. Slightly plastic; moderate cementation. Moist color: 10YR 3/2. 95% fines, 5% sand (very fine), 0% gravel, 0% cobbles/boulders
- Alluvial-fan sediment. Well bedded and moderately to well sorted sandy silt in the fault hanging wall. Sharp basal contact. Slightly plastic; no cementation. Moist color: 10YR 4/3. 80% fines, 20% sand (very fine–fine), 0% gravel, 0% cobbles/boulders
- C1 Scarp-derived colluvium. Weakly bedded and poorly sorted silty, sandy gravel diamict in the fault hanging wall. Sharp basal contact. Clasts are subangular to well rounded; 25 cm maximum; 8 cm average. Slightly plastic; poor cementation. Moist color: 10YR 5/4. 35% fines, 50% sand (coarse), 5% gravel, 10% cobbles/boulders
- Alluvial-fan sediment with paleosol. Massive and moderately sorted silty loam paleosol in the fault hanging wall. Diffuse basal contact. Clasts are subangular; 1 cm maximum; 1 cm average. Slightly plastic; moderate cementation. Moist color: 10YR 3/3. 90% fines, 5% sand (fine), 5% gravel, 0% cobbles/boulders

(continued)

### TABLE A1 (Continued)

#### Description Unit

- 32 Alluvial-fan sediment. Well bedded and moderately sorted silty sand in the fault hanging wall. Sharp basal contact. Nonplastic; no cementation. Moist color: 10YR 4/3. 30% fines, 70% sand (fine), 0% gravel, 0% cobbles/boulders
- 31 Alluvial-fan sediment with paleosol. Very weakly bedded and moderately sorted sandy, clayey silt paleosol(?) in the fault hanging wall. Irregular basal contact. Clasts are subangular; 3 cm maximum; 2 cm average. Very slightly plastic; moderate cementation. Moist color: 10YR 3/3. 70% fines, 25% sand (medium), 5% gravel, 0% cobbles/boulders
- Alluvial-fan sediment. Massive and poorly sorted clayey, gritty silt in the fault hanging wall. Diffuse basal contact. Clasts are subangular; 1.5 cm 20 maximum; 1 cm average. Plastic; moderate cementation. Moist color: 10YR 2/2. 75% fines, 20% sand (medium), 5% gravel, 0% cobbles/boulders
- C2 Scarp-derived colluvium. Moderately bedded and poorly sorted gravely, sandy silt/diamict in the fault hanging wall. Local slope-parallel clast fabric/ bedding. Sharp, faulted basal contact. Clasts are subangular to well rounded; 30 cm maximum; 8 cm average. Slightly plastic; poor cementation. Moist color: 10YR 4/2. 20% fines, 60% sand (coarse), 10% gravel, 10% cobbles/boulders
- Glaciofluvial sediment. Moderately bedded and poorly to moderately sorted silty, sandy gravel in the fault footwall. Basal contact not exposed. Clasts 10 are subangular to well rounded; 15 cm maximum; 4 cm average. Nonplastic; moderate cementation. Moist color: 10YR 3/2. 10% fines, 30% sand (medium-coarse), 60% gravel, 0% cobbles/boulders. Unit 10a exposed in fault hanging wall; unit 10b in footwall

Manuscript received 15 June 2020 Published online 8 December 2020